The Formation of Highly Positive δ^{34}S Values in Late Devonian Mudstones: Microscale Analysis of Pyrite (δ^{34}S) and Barite (δ^{34}S, δ^{18}O) in the Canol Formation (Selwyn Basin, Canada)

Haruna M. Grema [1,2]*, Joseph M. Magnall [1], Martin J. Whitehouse [3], Sarah A. Gleeson [1,2] and Hans-Martin Schulz [1]

[1]GFZ German Research Centre for Geosciences, Potsdam, Germany, [2]Institute of Geological Sciences, Freie Universität Berlin, Berlin, Germany, [3]Department of Geosciences, Swedish Museum of Natural History, Stockholm, Sweden

The sulfur isotope composition of pyrite in marine sedimentary rocks is often difficult to interpret due to a lack of precise isotopic constraints for coeval sulfate. This study examines pyrite and barite in the Late Devonian Canol Formation (Selwyn Basin, Canada), which provides an archive of δ^{34}S and δ^{18}O values during diagenesis. Scanning electron microscopy (SEM) has been combined with microscale secondary ion mass spectrometry (SIMS) analysis ($n = 1,032$) of pyrite (δ^{34}S) and barite (δ^{34}S and δ^{18}O) on samples collected from nine stratigraphic sections of the Canol Formation. Two paragenetic stages of pyrite and barite formation have been distinguished, both replaced by barium carbonate and feldspar. The $\delta^{34}S_{barite}$ and $\delta^{18}O_{barite}$ values from all sections overlap, between +37.1‰ and +67.9‰ (median = +45.7‰) and +8.8‰ and +23.9‰ (median = +20.0‰), respectively. Barite morphologies and isotopic values are consistent with precipitation from diagenetically modified porewater sulfate (sulfate resupply << sulfate depletion) during early diagenesis. The two pyrite generations (Py-1 and Py-2) preserve distinct textures and end-member isotopic records. There is a large offset from coeval Late Devonian seawater sulfate in the $\delta^{34}S_{pyrite}$ values of framboidal pyrite (-29.4‰ to -9.3‰), consistent with dissimilatory microbial sulfate reduction (MSR) during early diagenesis. The Py-2 is in textural equilibrium with barite generation 2 (Brt-2) and records a broad range of more positive $\delta^{34}S_{Py-2}$ values (+9.4‰ to + 44.5‰). The distinctive highly positive $\delta^{34}S_{pyrite}$ values developed from sulfate limited conditions around the sulfate methane transition zone (SMTZ). We propose that a combination of factors, including low sulfate concentrations, MSR, and sulfate reduction coupled to anaerobic oxidation of methane (SR-AOM), led to the formation of highly positive $\delta^{34}S_{pyrite}$ and $\delta^{34}S_{barite}$ values in the Canol Formation. The presence of highly positive $\delta^{34}S_{pyrite}$ values in other Late Devonian sedimentary units indicate that diagenetic pyrite formation at the SMTZ may be a more general feature of other Lower Paleozoic basins.

Keywords: sulfur isotopes, microscale SIMS analyses, anaerobic oxidation of methane, microbial sulfate reduction, sulfur cycling, Late Devonian

INTRODUCTION

Methane is a powerful greenhouse gas that is produced during the final stage of organic matter fermentation (Knittel and Boetius, 2009). Changes in the flux of methane (from sediment to oceans) have been linked with major climatic impacts at particular stages of earth history (e.g., Dickens et al., 1995). In modern ocean sediments, sulfate reduction coupled with the anaerobic oxidation of methane (SR-AOM) accounts for approximately 80% of methane oxidation, thereby regulating the release of methane into the atmosphere (Egger et al., 2018). Authigenic pyrite (FeS_2) and barite ($BaSO_4$) can both form as by-products of SR-AOM, meaning these phases provide a potential archive of methane oxidation (e.g., Borowski et al., 2013; Wood et al., 2021).

Pyrite and barite also provide an important archive for sulfur isotopes in marine environments, which can be used to reconstruct biogeochemical processes that link the sulfur, carbon, and iron cycles (Bottrell and Newton, 2006; Fike et al., 2015). For example, pyrite forms as a by-product of microbial sulfate reduction (MSR) during organoclastic sulfate reduction (OSR) and SR-AOM. There is a large isotopic fractionation associated with MSR, due to the differential reaction rates of the sulfate isotopologues ($^{32}S^{16}O_4 >$ $^{34}S^{18}O_4$; Kaplan and Rittenberg, 1964; Seal et al., 2000; Canfield, 2001a). As a result, pyrite often preserves $\delta^{34}S$ values that are offset relative to coeval seawater sulfate ($\delta^{34}S_{pyrite} << \delta^{34}S_{seawater}$; Fike et al., 2015). Stratigraphic variability in $\delta^{34}S$ values have been used to infer regional to global-scale changes in the sulfur cycle that reflect enhanced pyrite burial (e.g., Goodfellow and Jonasson, 1984) and the size of the marine sulfate reservoir (e.g., Kah et al., 2004).

More recently, studies have shown how sulfur isotope variability may instead be controlled by sedimentary facies and diagenetic processes (Magnall et al., 2016; Pasquier et al., 2017; Marin-Carbonne et al., 2018; Bryant et al., 2019; Richardson et al., 2019; Bryant et al., 2020; Pasquier et al., 2021). For example, the progressive modification of pore fluid sulfate by MSR during diagenesis can result in strong isotopic gradients and a range of $\delta^{34}S_{pyrite}$ values, depending on the location of pyrite formation in the sediment (Canfield, 2001b; Canfield et al., 2010). In particular, studies have benefited from the generation of isotopic data using microscale techniques (e.g., secondary ion mass spectrometry; SIMS), which enable the determination of paragenetically constrained phase specific $\delta^{34}S$ values. However, there are relatively few examples where $\delta^{34}S_{pyrite}$ and proxies for coeval $\delta^{34}S_{sulfate}$ values have been paired at high spatial resolutions (e.g., Magnall et al., 2016). As a result, the origin of highly positive or 'superheavy' $\delta^{34}S_{pyrite}$ values ($\delta^{34}S_{pyrite} > \delta^{34}S_{SO4}$; Ries et al., 2009) can be particularly difficult to constrain. For example, highly positive $\delta^{34}S$ values in pyrite in sedimentary units from the Late Devonian period have been linked with MSR in low sulfate water/sediment columns (Goodfellow and Jonasson, 1984; Sim et al., 2015; Zhang et al., 2020) or formation through hydrothermal or thermochemical sulfate reduction (TSR; Yan et al., 2020).

The Late Devonian was one of the major periods of organic carbon burial in earth history (Klemme and Ulmishek, 1991). In the Selwyn Basin, Canada, clastic-dominated type (CD-type) Zn-Pb ± Ba mineralization is hosted by Late Devonian mudstones
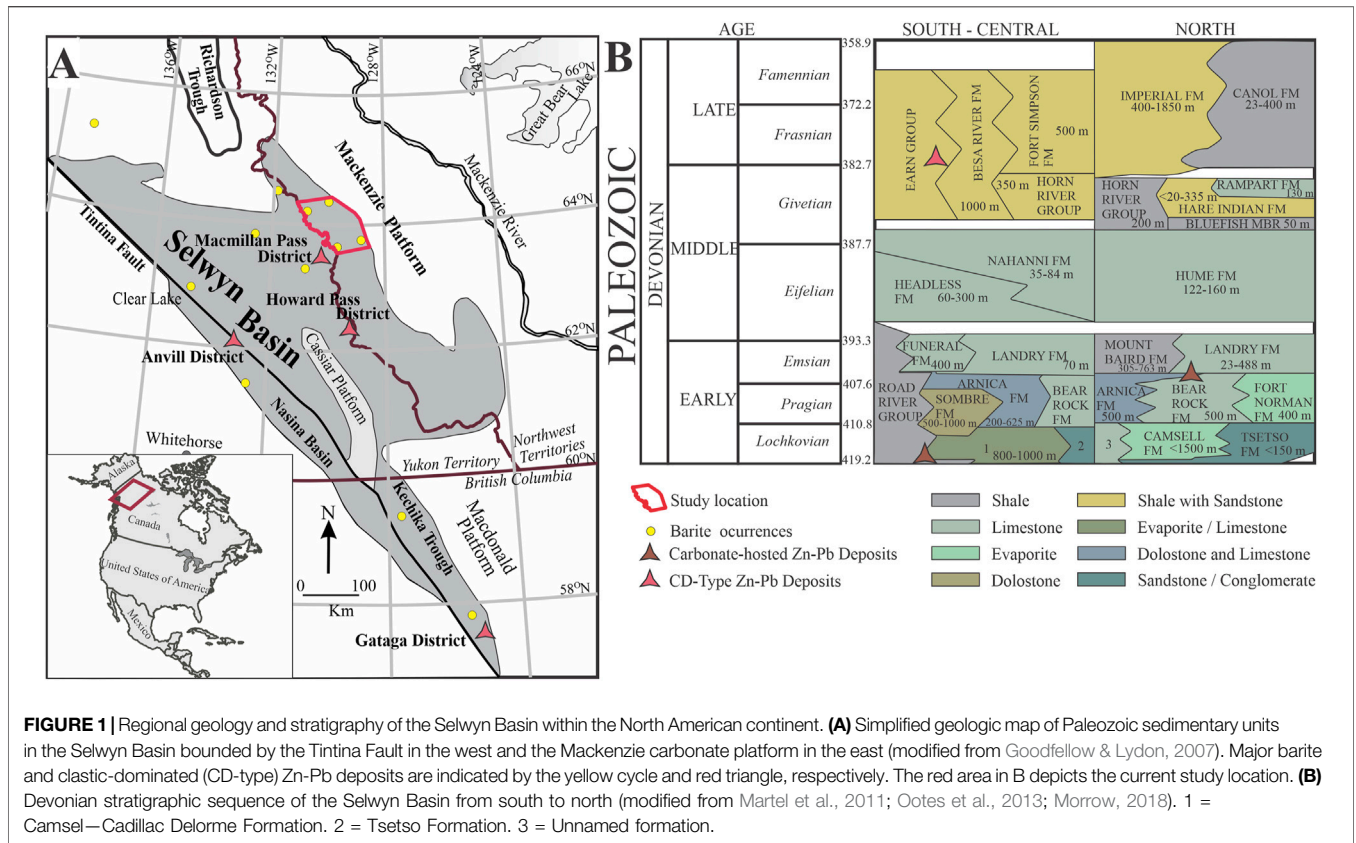
(Goodfellow and Jonasson, 1984; Goodfellow, 1987; Hanor, 2000; Johnson et al., 2009; Farquhar et al., 2010; Magnall et al., 2020b). Bedded barite is hosted by unmineralized Late Devonian mudstones in the Selwyn Basin (Fernandes et al., 2017), although the spatial association with the CD-type massive sulfide deposits meant the barite was considered to be a distal expression of sedimentary exhalative (SEDEX) hydrothermal activity (Large et al., 2005; Leach et al., 2005; Goodfellow and Lydon, 2007; Leach et al., 2010). In this SEDEX model, highly enriched $\delta^{34}S$ values in pyrite and barite have been interpreted to indicate nearly complete sulfate reduction during MSR in a stagnant and stratified anoxic water column (Goodfellow and Jonasson, 1984).

Recent studies, however, have highlighted how barite may have been formed by diagenetic processes before being subsequently replaced during hydrothermal sulfide mineralization (Johnson et al., 2009; Magnall et al., 2016; Johnson et al., 2018; Magnall et al., 2020a; Reynolds et al., 2021). In the diagenetic model, it is proposed that the barite formed in a setting analogous to cold seep environments where methane is oxidized by sulfate through microbial metabolic processes (Greinert et al., 2002; Paytan et al., 2002; Torres et al., 2003; Canet et al., 2014). The sulfate methane transition zone (SMTZ) is a diagenetic redox boundary in organic carbon-bearing sediments that is an important habitat for a consortium of sulfate-reducing and methanotrophic microorganisms (Torres et al., 1996; Machel, 2001; Arning et al., 2015). Organic matter is converted during early diagenesis in such sediments, and the water-soluble products (e.g., acetic acid, CO_2, and CH_4) change the porewater composition (e.g., pH), resulting in a series of hydrogeochemical reactions of dissolution (e.g., feldspar) and precipitation (e.g., barite). Diverse $\delta^{34}S_{barite}$ values have been recorded at modern cold seeps (up to ~40‰; Greinert et al., 2002; Wood et al., 2021) that are correspondingly similar to highly positive $\delta^{34}S$ values in Paleozoic bedded barite (Johnson et al., 2009; Canet et al., 2014). Such highly positive $\delta^{34}S_{barite}$ values are interpreted to result from the residual sulfate pool at the SMTZ (Canet et al., 2014; Clark et al., 2015). When methane oxidation is coupled to sulfate reduction at the SMTZ and in the presence of an iron source, pyrite is formed at the SMTZ, and this pyrite can have positive $\delta^{34}S_{pyrite}$ values (e.g., Borowski et al., 2013).

This study integrates high-resolution scanning electron (SEM) microscopy petrography of barite (+ associated barium phases) and pyrite, together with microscale isotopic microanalyses of $\delta^{34}S_{pyrite}$, $\delta^{34}S_{barite}$, and $\delta^{18}O_{barite}$ of selected samples from the Late Devonian Canol Formation of the Selwyn Basin. We have targeted samples containing both barite and pyrite to develop paired isotopic constraints on the evolution of sulfur during diagenesis. In particular, we have focused on the precise mechanism by which highly positive $\delta^{34}S_{pyrite}$ developed in the Canol Formation and discussed the implications for interpreting sulfur isotopes in similar settings.

REGIONAL GEOLOGY

The Selwyn Basin (**Figure 1A**) is primarily made up of Neoproterozoic to Mississippian, deep to shallow marine siliciclastics, and platform carbonate strata, deposited on the

FIGURE 1 | Regional geology and stratigraphy of the Selwyn Basin within the North American continent. **(A)** Simplified geologic map of Paleozoic sedimentary units in the Selwyn Basin bounded by the Tintina Fault in the west and the Mackenzie carbonate platform in the east (modified from Goodfellow & Lydon, 2007). Major barite and clastic-dominated (CD-type) Zn-Pb deposits are indicated by the yellow cycle and red triangle, respectively. The red area in B depicts the current study location. **(B)** Devonian stratigraphic sequence of the Selwyn Basin from south to north (modified from Martel et al., 2011; Ootes et al., 2013; Morrow, 2018). 1 = Camsel—Cadillac Delorme Formation. 2 = Tsetso Formation. 3 = Unnamed formation.

margin of the ancestral North American continent (Mair et al., 2006). Formation of the basin stems from widespread protracted extensional tectonics of the Rodinian supercontinent that led to the re-emergence of the Laurentian craton between 825 and 740 Ma (Martel et al., 2011) with resulting development of the epicontinental margin and Selwyn Basin during the Ediacaran—Cambrian periods (Gordey, 1993). The oldest strata in the basin consist of the syn-rift Neoproterozoic-Terreneuvian Windermere Supergroup overlain by basinal post-rift Paleozoic sedimentary rocks with a combined total thickness of around 7,500 m (Ootes et al., 2013). Abrupt episodic extensions and volcanism during the Early Cambrian, Middle Ordovician, and Devonian are characterized by mafic volcanics within the platform carbonate and the basinal strata (Goodfellow and Lydon, 2007). Collision with an island arc during the Late Devonian is suggested to have led to deformation and subsequent incorporation of the Selwyn Basin strata into the fold and thrust belt of the North American Cordillera (Mair et al., 2006). A sudden change in depositional regime during the Late Devonian led to the deposition of siliciclastic sediments that spread from the margin of Laurentia toward the interior of the craton (Martel et al., 2011). Together with an overlying turbidite unit, the siliciclastic sediments are collectively known as the Earn Group (**Figure 1B**; Gordey, 2013; Ootes et al., 2013).

The Earn Group is subdivided into an upper unit of coarse-grained siliciclastic turbidites and sandstones of the Imperial Formation and a lower Canol Formation (Martel et al., 2011). The Canol Formation is of Upper-Devonian (Frasnian—early Famennian) age and consists primarily of dark grey to black mudstones locally calcareous or siliceous with occasional carbonate concretions of variable sizes (Mair et al., 2006; Martel et al., 2011). The formation is extensively widespread in the Mackenzie Mountains region with variable thickness that reaches 400 m (Cecile et al., 1983; Martel et al., 2011; Gadd et al., 2016). The depositional setting of the Canol Formation has been interpreted to be of deep-water marine, formed during the early stages of foredeep basin development (Cecile et al., 1983).

Local Geology

This study builds on an earlier study by Fernandes et al. (2017) located northeast of the Macmillan Pass district (**Figure 1A**). The sedimentary rocks of the Canol Formation in the study area consist of gently open-folded, bedded coarser-grained siliciclastics and organic-rich mudstones that are moderate to steeply dipping and weathering to silver color (Fernandes, 2011; Fernandes et al., 2017). These lithologic units host several stratiform barite beds that form barite horizons in equivalent Devonian stratigraphic intervals on a regional scale (e.g., Goodfellow and Jonasson, 1984; Smith et al., 1993; Magnall et al., 2016; Fernandes et al., 2017).
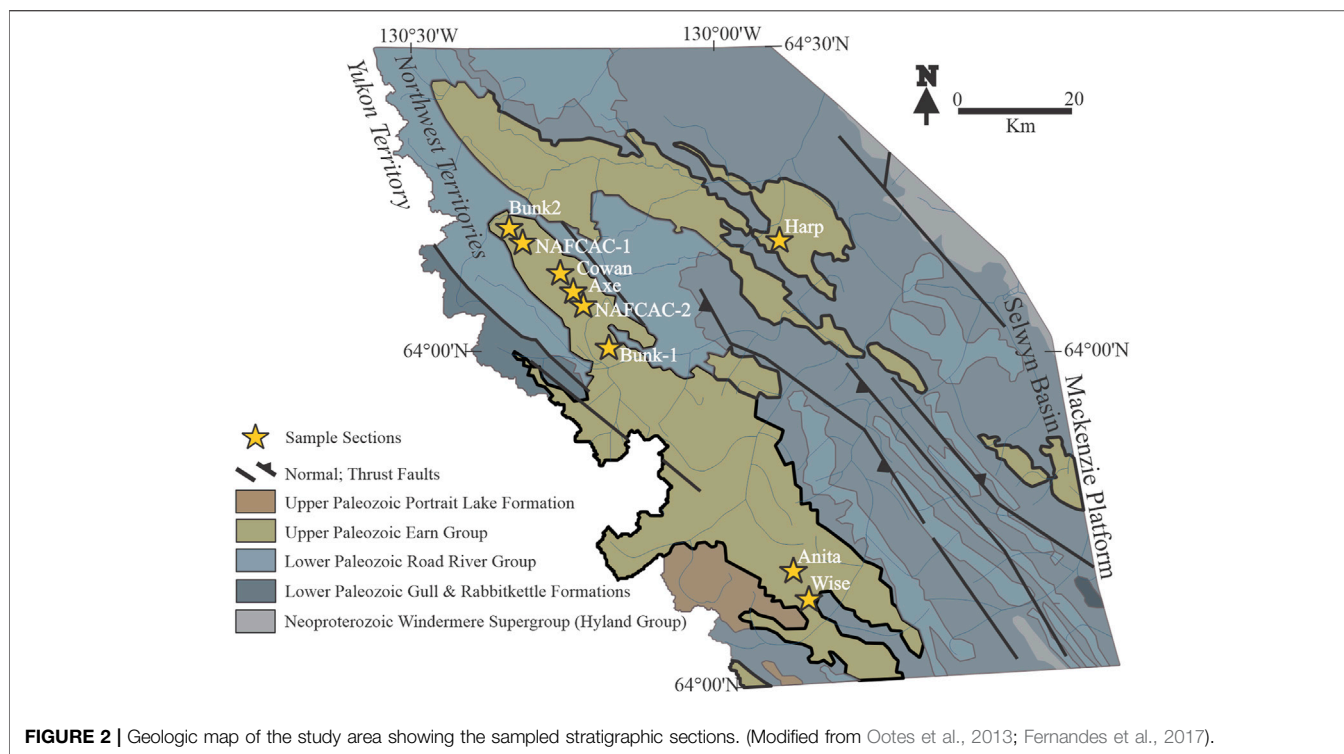
FIGURE 2 | Geologic map of the study area showing the sampled stratigraphic sections. (Modified from Ootes et al., 2013; Fernandes et al., 2017).

In the Northwest Territories' part of the Selwyn Basin, 22–72 m thick barite sequences occur within stratigraphic sections at Bunk-2, Bunk-2, Cowan, NAFCAC-1, NAFCAC-2, Anita, Axe, Harp, and Wise locations (**Figures 2**, **3**; Fernandes et al., 2017). These barite-bearing sections occur as topographic highs, in a broad 200 km long NW-SE trend, are all confined to the upper parts of the Canol Formation, below the unconformity with the fine-grained siliciclastics of the Imperial Formation and are considered to be Frasnian in age (Martel et al., 2011; Fernandes et al., 2017). Mineralogically, the mudstones consist of varying amounts of clay minerals, quartz, and organic matter, with barite, pyrite, and Ba-bearing feldspar (hyalophane (K, Ba) [Al (Si, Al)$_3$O$_8$] and cymrite BaAl$_2$Si$_2$(O, OH)$_8$ · H$_2$O) constituting the major accessory minerals (Fernandes, 2011). Fernandes et al. (2017) further describe the intricate relationship between barite and Ba-bearing carbonates and silicates; witherite (BaCO$_3$) forms a textural association with barite, replacing both laminated and nodular barite grains, while hyalophane and cymrite are 0.5–2 mm crystals found replacing barite and witherite in both the laminae and nodules (Fernandes et al., 2017).

Bedded Barite Mineralization Style in the Canol Formation

There are two types of barite (laminated and nodular) identified in the upper Canol Formation that occur interlaminated together; nodular barite was dominant over laminated form (**Figure 3**; Fernandes et al., 2017). Brief descriptions of the barite forms from Fernandes et al. (2017) are highlighted below and shown in **Figure 4**.

The barite nodules in mudstones are spherical, ellipsoidal, or irregular (**Figures 4A–C**). The nodules often contain barite crystals

that are rosette or tabular with a size range from less than 100 µm to 1.2 cm (**Figure 4E**). Witherite, hyalophane, cymrite, and quartz are associated primarily with the barite crystals (**Figures 4G,H**). The laminated barite has been described to primarily occur as clusters of intergrown anhedral crystals within 50–100 µm laminae (e.g., **Figure 4D**). Associated minerals include pyrite, cymrite, quartz, and hyalophane with intercalated clay-rich laminae (**Figure 4H**). Grey mudstone with about a meter of laminated and nodular barite occurs in the Bunk-2 section between dark grey siltstone hosting nodular barite (**Figure 4I**). The barite crystals range from <10 to 70 µm, either concordant with the lamina or irregular with no specific direction.

METHODOLOGY

Sampling

Sixty-five (65) mudstone samples from the nine barite-bearing sections from the suite of samples investigated by Fernandes (2011) were resampled. Samples containing pyrite and barite were targeted, and their mineralogical and paragenetic relationships were examined using binocular microscopy as a first step.

Petrography

Detailed petrographic examination of the mineralogical and textural relationships was carried out on thin sections using an Olympus BX51 microscope, equipped with a Sc50 camera, in transmitted and reflected light settings. Polished thin sections were additionally prepared and carbon-coated to a thickness of 20 nm for further examination and imaging using an electron
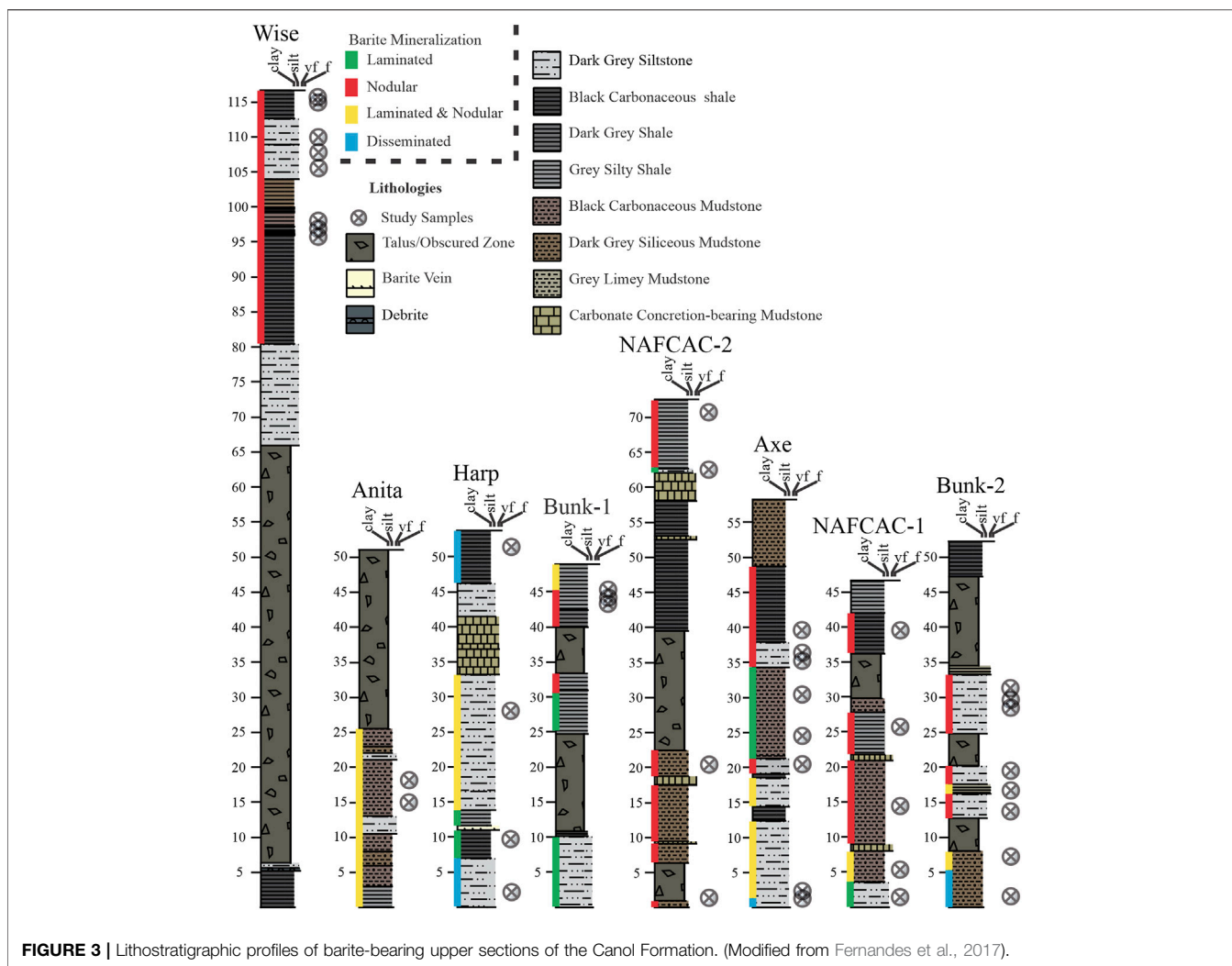
FIGURE 3 | Lithostratigraphic profiles of barite-bearing upper sections of the Canol Formation. (Modified from Fernandes et al., 2017).

probe microanalyzer (EPMA) and SEM. Backscatter electron images (BSE) were obtained using Japan Electron Optics Limited (JEOL) JXA-8530F Hyperprobe, equipped with a wavelength and energy dispersive spectrometry combined system. The EPMA was operated using a beam diameter between 1 and 3 μm, beam current of 15 nA, and accelerating potential of 15 kV, in secondary electron (SE) and BSE modes. Organic petrography using a standard reflection microscope showed that randomly distributed organoclasts occur as < 2 μm sized particles. Due to the thermal overmaturity, the particles are inertinite and prevent a broader reconstruction of organic matter type.

Secondary Ion Mass Spectrometry (SIMS) Analyses of Sulfur and Oxygen Isotopes

Microdrills of regions of interest (n = 54) were made on polished sections to obtain suitable subsamples, using a 4 mm diameter diamond core drill, from the whole sample suite in Fernandes (2011). Several representative subsamples

were cast into 25 mm epoxy pucks, together with reference materials (RMs) of pyrite S0302A (δ^{34}S $_{V\text{-}CDT}$ = 0.0 ± 0.2‰; Liseroudi et al., 2021) and barite S0327 (δ^{34}S$_{V\text{-}CDT}$ = 11.0 ± 0.5‰; δ^{18}O$_{V\text{-}SMOW}$ = 21.3 ± 0.2‰; Magnall et al., 2016). Re-examination and further BSE imaging were carried out with EPMA after carbon-coating, with subsequent 30 nm gold coating added to the mounts before isotope measurement. Microscale isotopic analyses were carried out using Cameca IMS1280 large-geometry secondary ion mass spectrometer (SIMS) operated in multi-collector mode at the NordSIMS laboratory, Stockholm, Sweden. For the measurements, a ^{133}Cs$^+$, 20 kV impact energy primary beam was utilized. The beam current was 1 nA for all barite analyses, and the larger pyrite targets, yielding a ca. 10 μm spot; a 400—500 pA beam was used for smaller pyrite targets yielding a ca. 6 μm spot. A normal incidence low-energy electron flooding gun was utilized for charge compensation. Sulfur and oxygen isotopes were determined in separate analytical sessions in which secondary ion signals of ^{32}S and ^{34}S or ^{16}O and ^{18}O were measured simultaneously in two Faraday cups.
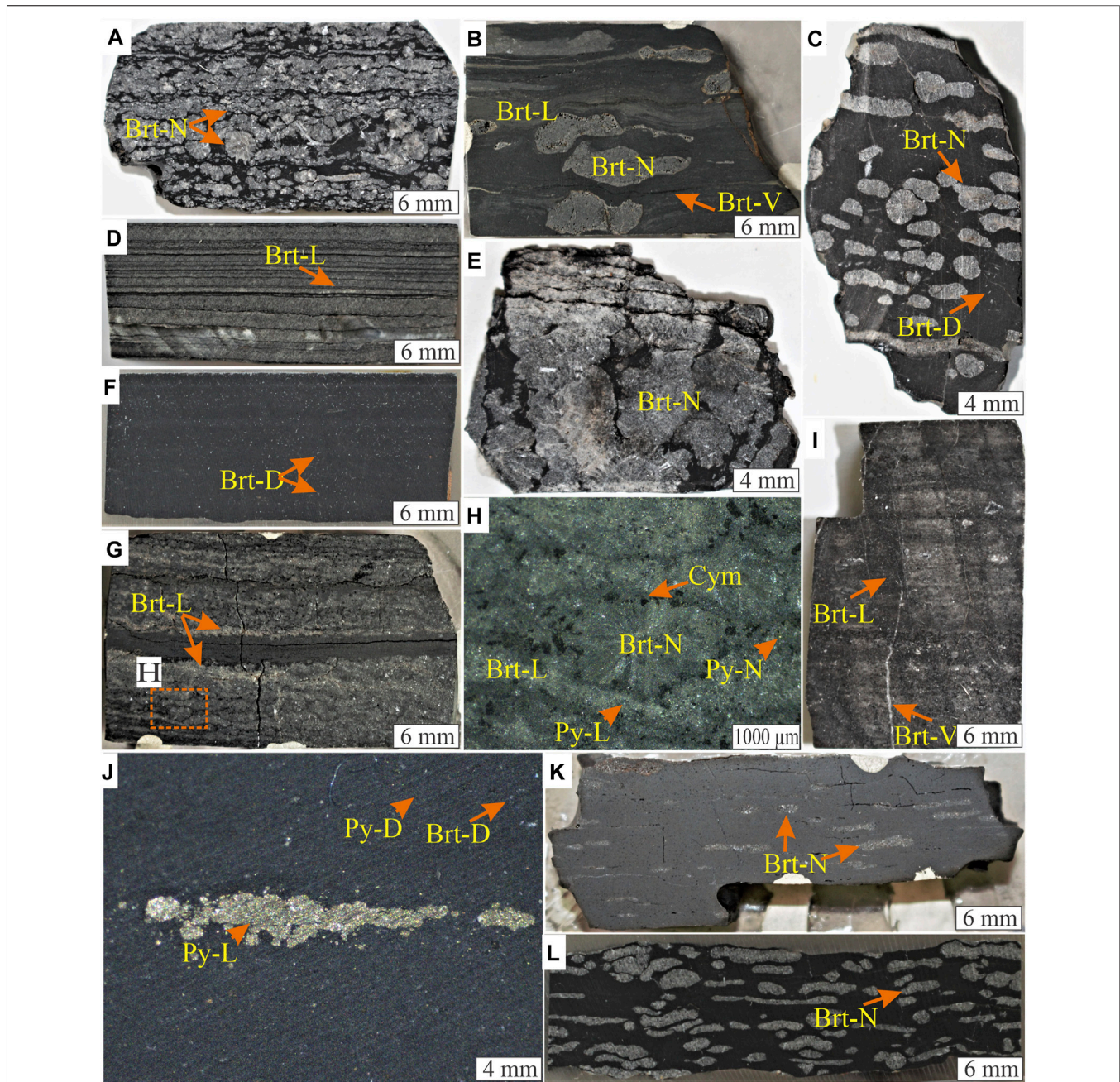
FIGURE 4 | Representative hand specimen and binocular photographs of mudrocks showing different forms of barite mineralization. **(A)** Black carbonaceous mudstone with nodular barite grains (Brt-N). **(B)** Dark grey shale with thin barite laminations (Brt-L) and nodular (Brt-N) irregular barite grains. Dark grey barite veins (Brt-V) are observed to have formed parallel to the bedding. **(C)** Dark grey siliceous mudstone showing nodular barite. **(D)** Grey siliceous shale with thinly laminated barite. **(E)** Large barite nodules within dark grey siltstone. **(F)** Black carbonaceous mudstone. Disseminated barite (Brt-D) is commonly associated with anhedral quartz grains. **(G)** Laminated and rosette nodular barite with stratiform pyrite and barite are intergrown with cymrite (cym) in **(H)**. **(I)** Rare lime dark grey mudstone with discordant barite vein. **(J)** Binocular microscope photograph of black mudstone with disseminated pyrite (Py-D) and aggregates of stratiform pyrite (Py-L). **(K)** Dark grey siliceous shale showing ellipsoidal barite nodules parallel to the bedding. **(L)** Highly irregular barite nodules in black carbonaceous shale.

A total of 1,032 sulfur and oxygen isotope measurements ($\delta^{34}S_{pyrite}$ = 200; $\delta^{34}S_{barite}$ = 485, $\delta^{18}O_{barite}$ = 338) on pyrite and barite grains were obtained using automated analytical sequences in which every 6 to 7 measurements are followed by 1–2 RM analyses. The $\delta^{34}S_{barite}$ and $\delta^{18}O_{barite}$ values measurements were carried out on the same

barite grains to capture the covariation between the sulfur and oxygen isotopic systems. Within-session drift and instrumental mass fractionation (IMF) were corrected using the regularly interspersed analyses of the RMs in each session. The IMF-corrected $^{34}S/^{32}S$ ratios are reported relative to Vienna Canyon Diablo Troilite (V-CDT) and

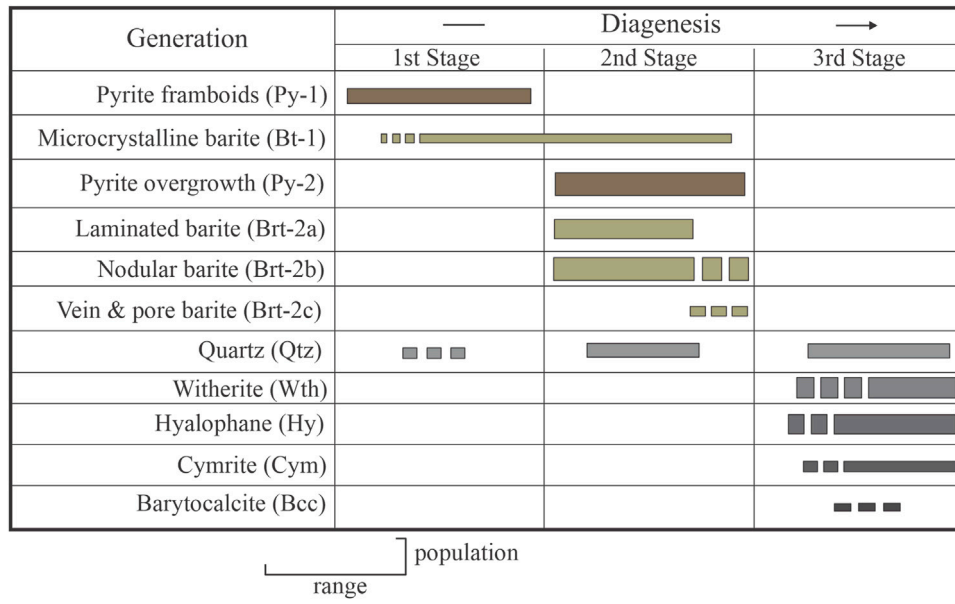| Generation	Diagenesis		
	1st Stage	2nd Stage	3rd Stage
Pyrite framboids (Py-1)	▬▬▬▬		
Microcrystalline barite (Bt-1)	▪▪▪ ▬▬▬▬▬▬		
Pyrite overgrowth (Py-2)		▬▬▬▬▬	
Laminated barite (Brt-2a)		▬▬▬	
Nodular barite (Brt-2b)		▬▬▬ ▪ ▪	
Vein & pore barite (Brt-2c)		▪ ▪ ▪	
Quartz (Qtz)	▪ ▪ ▪	▬▬▬	▬▬▬▬▬
Witherite (Wth)			▪▪▪ ▬▬
Hyalophane (Hy)			▪▪ ▬▬▬▬
Cymrite (Cym)			▪▪ ▬▬▬
Barytocalcite (Bcc)			▪ ▪ ▪

population
range

FIGURE 5 | Simplified paragenetic succession of main pyrite and barite generations.
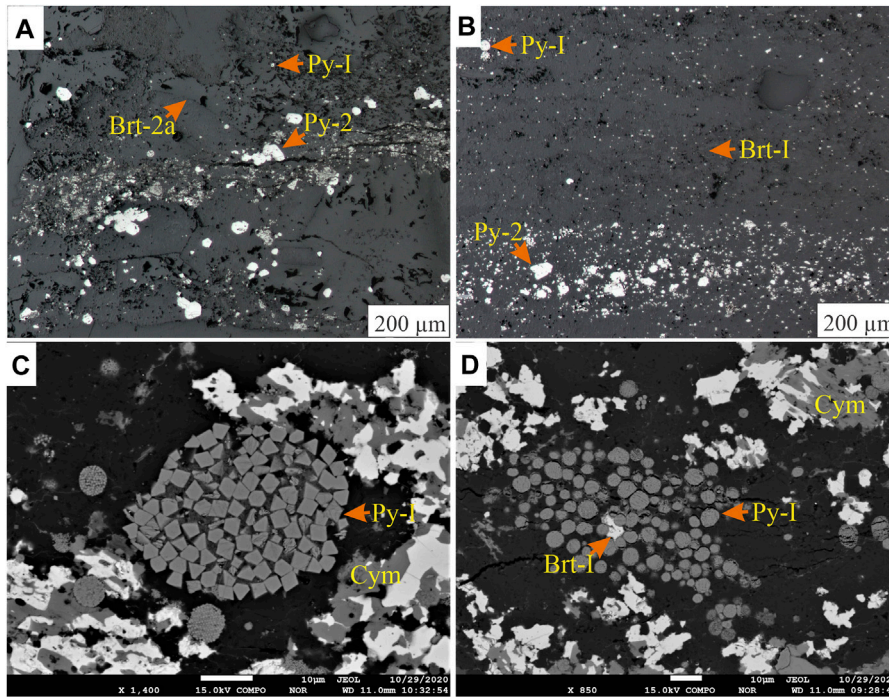
FIGURE 6 | Reflected light and backscatter electron (BSE) images of pyrite and barite generations. **(A)** Reflected light image showing pyrite framboids (Py-1) in intra- and intergranular pores spaces of barite (Brt-2a) and clay matrix. Pyrite (Py-2) is observed to be disseminated within the matrix and in and around interlocking grains of laminated barite (Brt-2a). **(B)** Reflected light image of stratiform pyrite (Py-2) in clay lamination with microcrystalline barite (Brt-1) and pyrite framboids (Py-1). **(C)** BSE image of pyrite framboids (Py-1) of variable sizes and nanocrystal morphologies within carbonaceous mudrock matrix. **(D)** BSE image of Py-1 framboids and polyframboids with disseminated microcrystalline barite (Brt-1) and replaced mainly by cymrite (Cym).
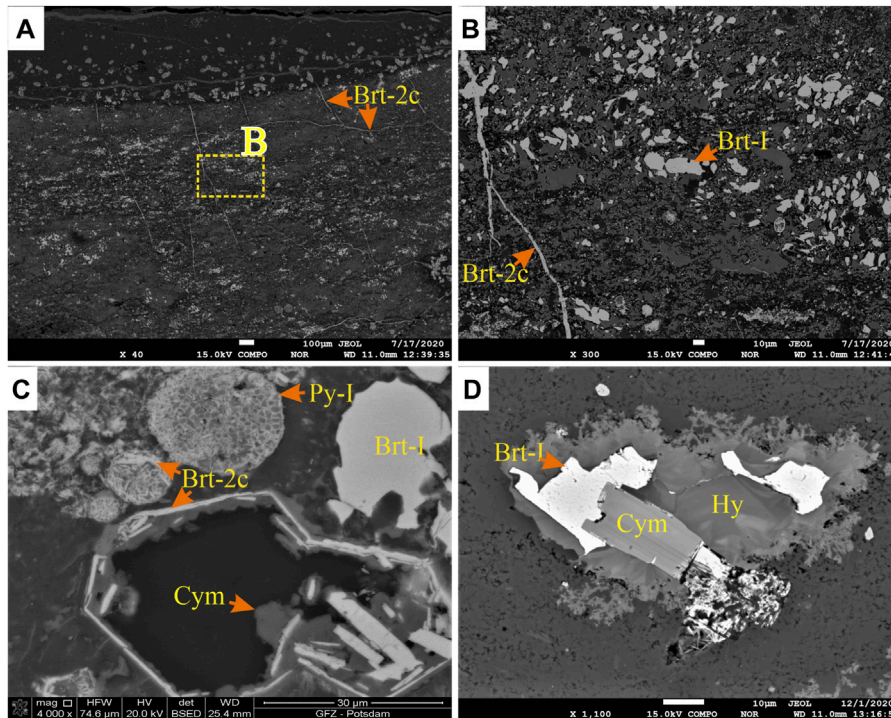
FIGURE 7 | (A) BSE image of barite crystals with barite veins (Brt-2c). The orange box depicts BSE image B. **(B)** BSE image of barite vein (Brt-2c) crosscutting earlier formed barite grains, including microcrystalline barite (Brt-1). **(C)** SEM BSE image of barite replacement of framboidal pyrite (Py-I) by Brt-2c. Cymrite (Cym) grows in the pore spaces left by the dissolution of pyrite (Py-2) grains. **(D)** BSE image of Brt-I intergrowth with cymrite (Cym) and within subhedral and dendritic hyalophane (Hy).

^{18}O/^{16}O ratios relative to Vienna Standard Mean Ocean Water (V-SMOW), using conventional delta notation:

$$\delta^{34}S \ (‰, \ V-CDT) = \left[\left(\frac{(^{34}S/^{32}S) \ sample}{(^{34}S/^{32}S) \ V-CDT} \right) - 1 \right] \times 1000$$

$$\delta^{18}O \ (‰, \ V-SMOW) = \left[\left(\frac{(^{18}O/^{16}O) \ sample}{(^{18}O/^{16}O) \ V-SMOW} \right) - 1 \right] \times 1000$$

External analytical reproducibility (1 σ) was typically ±0.04‰ $\delta^{34}S$ for pyrite, ± 0.15‰ $\delta^{34}S$, and ±0.12‰ $\delta^{18}O$ for barite. The reproducibility for each session is the standard deviation of the reference material measurements in that session. For any individual measurement, the external uncertainty is propagated together with the within-run uncertainty for an overall value. Post SIMS SEM imaging was carried out on each barite and pyrite spot for confirmation of target integrity; measurements on pyrite-barite grain boundaries were discarded ($n = 14$).

RESULTS

Mineralogy and Paragenesis

Different pyrite and barite formation stages have been defined in terms of shape, size, and distribution, broadly comparable across the different stratigraphic intervals (**Figure 5**). The different stages of pyrite and barite are described in terms of their relative timing of formation (paragenesis). Detailed descriptions are given below.

Stage 1: The earliest stage of pyrite (Py-1) comprises framboids present in all the sections (apart from NAFCAC-2 and Anita). Framboidal pyrite is particularly enriched in the mudstones of Harp and Axe sections. Py-1 is commonly located in the inter-and intra-granular pore space of the mudstone laminae and nodules (**Figures 6A,B**). The framboids have a broad size distribution, mostly <45 μm (**Figure 6C**), although spherical to irregular clusters of polyframboids reach up to 80 μm in diameter (**Figure 6D**). The individual framboid microcrystals are <5 μm, mostly equant, cubic, or pyritohedral (**Figure 6C**). The first stage of barite (Brt-1) is microcrystalline, <35 μm with subhedral to euhedral disseminated grains, and is found in mudstones in all sections. The Brt-1 is intergrown with quartz and cymrite in clay-rich or quartz-dominated matrices (**Figures 7A–D**). The Brt-1 and Py-1 grains rarely occur together, and establishing their paragenetic relationship was consequently difficult.

Stage 2: The second stage, pyrite (Py-2), forms porous, subhedral to idiomorphic grains, primarily concentrated in laminae and nodules of the mudstones (**Figures 8A,B**). In the lower part of the Harp section, where the mudstones contain no barite laminae or nodules, Py-2 either occurs as disseminated crystals (<70 μm) or forms aggregates that are up to 2.7 mm
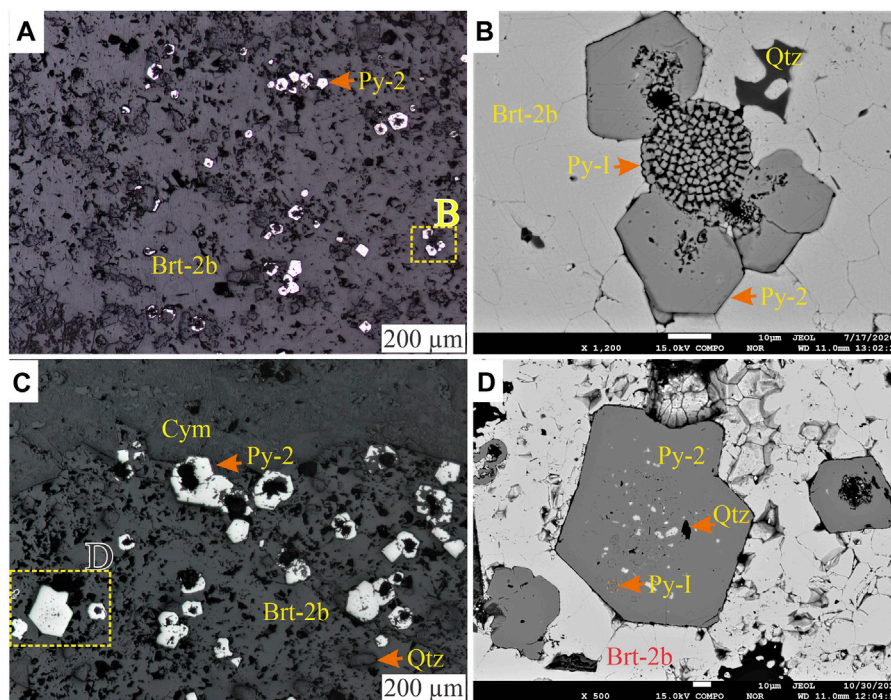
FIGURE 8 | (A) Reflected light photomicrograph of nodular barite (Brt-2b) with interlocking grains and intergrowing subhedral to euhedral pyrite (Py-2). **(B)** BSE image of the highlighted region in A showing the intergrowth relationship between Py-2 and Brt-2b. **(C)** Reflected light photomicrograph of Py-2 with porous cores that contain Py-1, barite, and quartz (quartz) inclusions, better highlighted in BSE image **(D)**.

(**Figure 4J**). The Py-2 grains sometimes form overgrowths on Py-1 and may contain inclusions of framboids, quartz, and barite (**Figures 8C,D**). Barite (Brt-2) forms subhedral to anhedral stratiform barite crystals (Brt-2a, **Figure 9A**) and spherical to irregular barite nodules (Brt-2b, **Figure 9B**). Together with other barium phases, this barite replaces the earlier formed Brt-1 (**Figures 6D, 7B**). The Brt-2a mainly occurs as well-formed horizontal (**Figure 4D**) and wavy to irregular laminae with intercalations of clay-rich laminae (**Figure 9A**), nodular Brt-2b is the dominant form of barite in the samples (**Figure 9C**). The Brt-2a laminae tend to wrap around rosette and nodules of Brt-2b when they occur together, associated with witherite, quartz, hyalophane, and cymrite (**Figures 9D–F**). Importantly, Brt-2b is intergrown with Py-2 with clear planar crystal boundaries, suggesting coprecipitation (e.g., **Figures 8B,D**). Notably, Brt-2 and Brt-1 are replaced by witherite, mainly in the dark grey mudstones of Harp, Cowan, and Axe sections. The vein and pore-filling barite (Brt-2c) comprises precipitation in the pore, intergranular spaces, and fractures and is most commonly observed in the Axe, NAFCAC-1, and Harp sections. Barite-2c tends to form replacement and feeder (conduits) textures, including veins, veinlets, lensoids, and idiomorphic barite crystals overgrowing or replacing earlier formed barite and pyrite and cymrite grains (**Figures 7B, 10**).

Stage 3: The third stage in the paragenesis comprises Ba-bearing minerals, including cymrite and hyalophane, precipitating as pseudomorphs of earlier formed mineral phases (**Figure 7C**). In essence, the formation of cymrite and hyalophane, together with witherite and quartz, continues after the precipitation of Py-2 and Brt-2 (**Figure 10C**).

Sulfur and Oxygen Isotopes in Pyrite and Barite

The results of the SIMS analyses of the isotopic compositions of pyrite and barite are provided in Grema et al. (2021) and presented in **Figures 11**, **12**. Pyrite has a large range of $\delta^{34}S$ values (**Figures 11**, **13**). Framboidal pyrite (Py-1) preserves mostly negative $\delta^{34}S$ values (**Figure 13A**), between −29.4‰ and −9.4‰, with a mean $\delta^{34}S$ value of −21.0 ± 6.3‰ (1σ, n = 23). Pyrite-2 preserves more positive $\delta^{34}S$ values (**Figure 13B**) between +9.4‰ and +44.5‰ and the mean is +31.0 ± 7.7‰ (1σ, n = 177).

The $\delta^{34}S_{barite}$ values in this study overlap (**Figure 12A**) and range between + 37.1‰ and + 67.9‰ (+51.1 ± 7.7‰, 1σ) with an outlier of + 15.3‰ from the mudstones of the NAFCAC-2 section. Measured $\delta^{18}O_{barite}$ values from the sections also overlap and are between + 8.8‰ and + 23.9‰ (+21.0 ± 1.7‰, 1σ). The Brt-2a $\delta^{34}S$ values are between + 37.1‰ and + 60.1‰ with a mean $\delta^{34}S$ value of +49.2 ± 4.7‰ (1σ, n = 63). Corresponding $\delta^{18}O$ values of +19.5‰ to + 23.7‰ with mean $\delta^{34}S$ value of +21.8 ± 1.5‰ (1σ, n = 24) are preserved in the Brt-2a barite (**Figure 12A**). The $\delta^{34}S$ and $\delta^{18}O$ values of Brt-2b (+ 51.4 ± 8.1‰, 1σ) are between + 38.8‰ and +67.9‰ (n = 391)
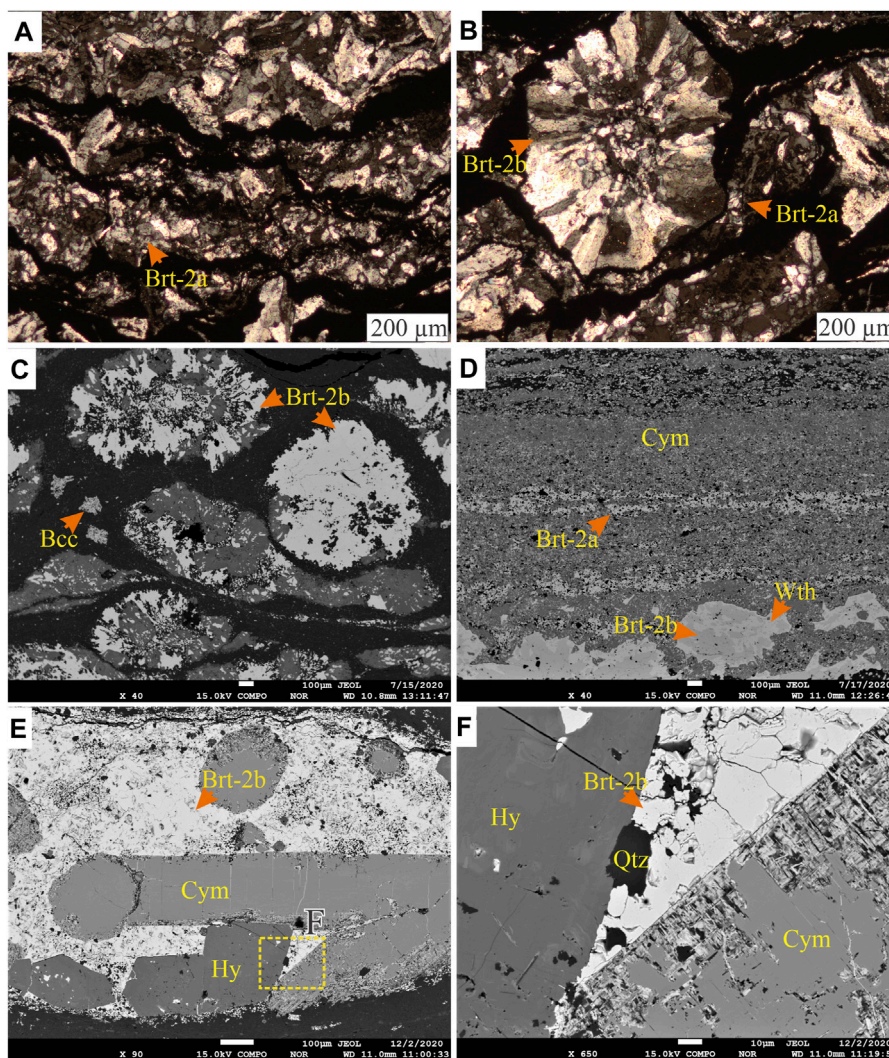
FIGURE 9 | (A) Transmitted light photomicrograph of kinked laminations of stratiform barite (Brt-2a) intercalated with clay-rich laminae. (B) Transmitted light photomicrograph in cross-polarized light of laminated barite (Brt-2a) wrapping around nodular barite (Brt-2b) grain. (C) BSE image of spherical and ellipsoidal Brt-2b with quartz intergrowth replaced by cymrite (Cym). Minor barytocalcite (Bcc) crystals are observed as spongy crystals within the matrix. (D) BSE image of laminated barite (Brt-2a) and nodular barite (Brt-2b). Brt-2b are replaced mainly by witherite, similar to the Ba-carbonate replacement of Brt-2a observable in the laminations. (E) BSE image of a nodule with subhedral to idiomorphic cymrite (Cym) and hyalophane (Hy) crystals in barite (Brt-2b). (F) BSE image of the area highlighted in image E showing the boundary relationship between the minerals present. The cymrite is seen being replaced from the margins by acicular barite and nanocrystals of quartz.

and +8.8‰ to +23.9‰ (+21.0 ± 1.7‰, 1σ, n = 284) respectively, with an outlier of $\delta^{18}O$ value of −5.5‰ (corresponding $\delta^{34}S$ value of + 40.1‰). The Brt-2b barite from the Cowan and NAFCAC-2 sections record the highest $\delta^{34}S$ values between + 60.8‰ and + 67.9‰, with corresponding $\delta^{18}O$ values between +18.4‰ and +23.5‰ (**Figure 12A**). Analyses of barite veins produced $\delta^{34}S$ values between + 44.4 and + 51.1‰ (+48.5 ± 3.6‰, 1σ) and $\delta^{18}O$ values between + 16.6‰ and + 21.5‰ (+19.5 ± 2.6‰, 1σ) respectively. Overall, there is observed covariation (**Figures 13C,D**) between $\delta^{34}S_{barite}$ and $\delta^{18}O_{barite}$ values, as indicated by the coefficient of determination (r^2 = 0.52; **Figure 12A**).

DISCUSSION

The mineralogical paragenesis and microscale isotopic constraints for pyrite and barite enable the reconstruction of the sulfur cycle during the deposition of the Canol Formation in the Late Devonian. The paired isotope data ($\delta^{34}S_{pyrite}$, $\delta^{34}S_{barite}$, and $\delta^{18}O_{barite}$) can be used to unravel the fate and behavior of the archived sulfate and to interpret the end-member $\delta^{34}S_{pyrite}$ values. In particular, the highly positive values occur in samples from several regionally correlative sections; this suggests the formation of these distinctive isotopic values could represent a regionally important (> 10 s km) process during the Late Devonian Selwyn Basin.
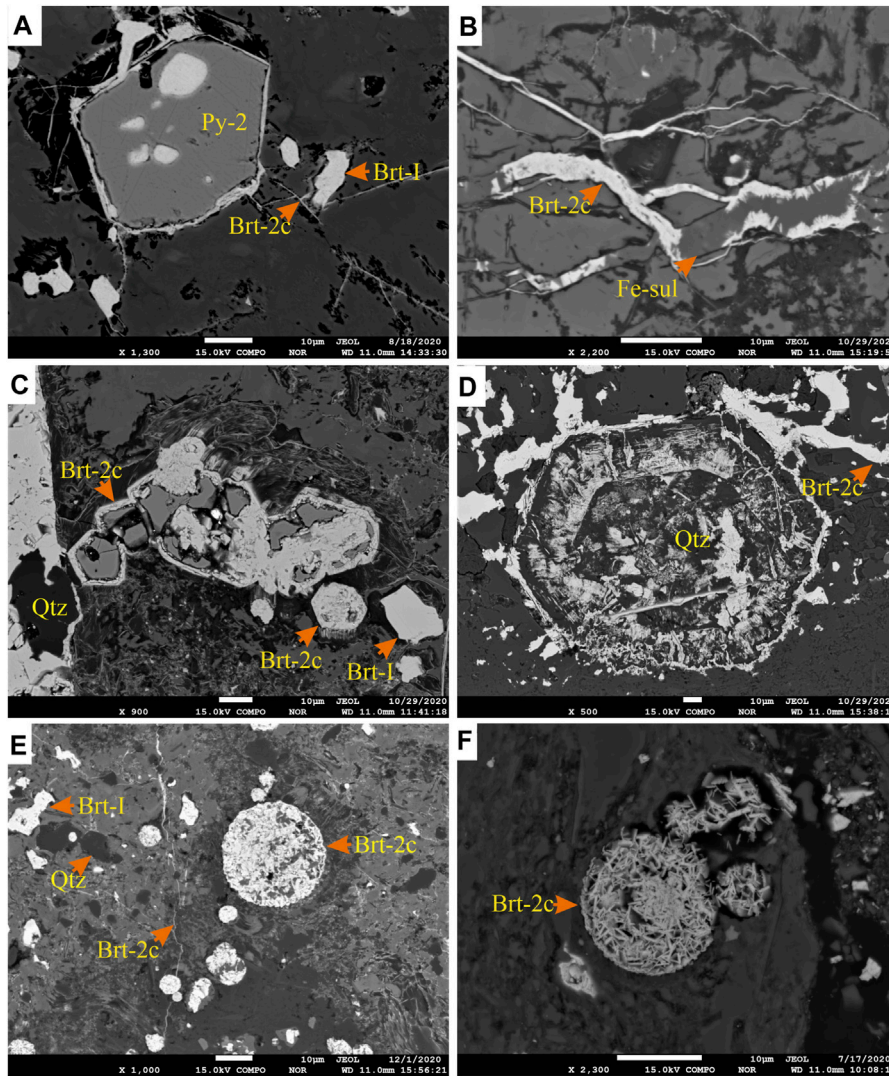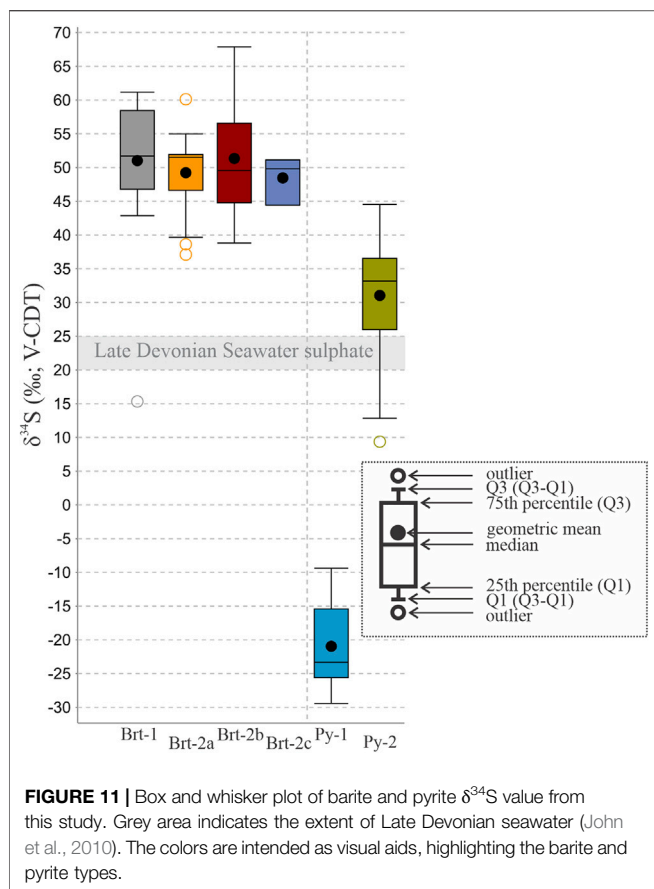
FIGURE 10 | (A) BSE image of Py-2 pyrite crystal with pores filled by barite. Barite veins (Brt-2c) are observed to rim the crystal. **(B)** Barite and iron-sulfate vein that appear to rim earlier formed minerals, as seen in image **(A)**. **(C)** BSE image of the progressive replacement of pyrite (Py-2) by barite (Brt-2c), that subsequently replace the pyrite grain but retaining the morphology of the mineral. **(D)** acicular barite pseudomorph retaining the replaced euhedral quartz habit. **(E)** BSE image of barite vein (Brt-2c) crosscutting and replacing pyrite framboids (Py-1). **(F)** Py-1 framboids completely replaced by euhedral microcrystals of barite, suggested to have progressed from the process observed in images **(C)** and **(E)**.

Barite Formation

The formation of pelagic barite in marine environments is initially associated with sinking particulate organic matter (Paytan et al., 2002; Gonzalez-Muñoz et al., 2012; Martínez Ruíz et al., 2020), which may then be recycled under reducing conditions during diagenesis (Torres et al., 1996). Under open-system conditions, biogenic barite preserves $\delta^{34}S$ and $\delta^{18}O$ values that represent unmodified seawater sulfate (Paytan and Griffith, 2007; Griffith and Paytan, 2012). The constraints for unmodified Late Devonian seawater sulfate ($\delta^{34}S$ values = 20 and 25‰; $\delta^{18}O$ values = 10–16‰) are provided by analyses of carbonate associated sulfate (CAS) from the Frasnian-Famennian boundary (John et al., 2010; Chen et al., 2013). However, the barite from all stratigraphic sections in this study

preserves higher $\delta^{34}S_{barite}$ values (median = 45‰), representing a substantial offset from Late Devonian seawater sulfate (**Figure 11**). Barite crystals with variable isotopic ratios are not restricted to a single section, depth, or lithology; the analyses reveal isotopic heterogeneity within and between grains of the same barite generation that are only a few microns apart (**Figures 13B–D**). This lack of isotopic distinction between the different barite types and the distribution of the isotopically heterogenous barite within the lithologies and sections may indicate a similar environment of formation across all stratigraphic sections (e.g., Magnall et al., 2016; **Figure 12B**).

The size (>5 μm) and morphology of the barite crystals are also consistent with barite precipitation in diagenetic pore

FIGURE 11 | Box and whisker plot of barite and pyrite δ^{34}S value from this study. Grey area indicates the extent of Late Devonian seawater (John et al., 2010). The colors are intended as visual aids, highlighting the barite and pyrite types.

fluids (Paytan et al., 2002; Paytan and Griffith, 2007). The two barite generations (Brt-1 and Brt-2) are isotopically indistinct (**Figure 12A**), despite paragenetic relationships that suggest barite precipitation during two stages (**Figures 6**, **9**). Both generations of barite are also surrounded by the siliciclastic and organic-rich host mudstones suggesting formation in early diagenesis near the seafloor (Aplin and Macquaker, 2011). The formation of the barite nodules (Brt-2b) might have coincided with increased compaction of the sediments, with clay minerals and organic matter dehydration possibly causing the nodules to form into ellipsoidal and irregular shapes (e.g., **Figure 9C**), parallel to the bedding plane (Goldberg et al., 2006; Paytan and Griffith, 2007; Zan et al., 2020).

Diagenetic barite formation is generally associated with the sulfate methane transition zone (SMTZ), where opposing diffusional fluxes of methane and sulfate interact (Barnes and Goldberg, 1976; Reeburgh, 1976; Jørgensen and Kasten, 2006). Barium is soluble in the strongly reducing CH_4-bearing fluids but will form diagenetic barite upon mixing with downward diffusing sulfate (Torres et al., 1996; Dickens, 2001). The depth of diagenetic barite formation and the degree to which pore fluid sulfate has been modified via MSR will significantly influence $\delta^{34}S_{barite}$ and $\delta^{18}O_{barite}$ values (Bottrell and Newton, 2006; Goldberg et al., 2006; Antler et al., 2013). Compared to the mineral separate analyses from the previous study (Fernandes

et al., 2017), the microscale $\delta^{34}S_{barite}$ and $\delta^{18}O_{barite}$ values in this study are biased towards an end member that represents strongly modified seawater (**Figure 12B**). Samples containing both pyrite and barite were targeted in this study, meaning the barite only samples that contained lower $\delta^{34}S_{barite}$ and $\delta^{18}O_{barite}$ values are underrepresented in the microscale dataset. Nevertheless, when interpreted together, the bulk rock and microscale data plot along a consistent trend (**Figure 12B**) that is typical of the progressive modification of seawater sulfate via MSR (e.g., Antler et al., 2013; Pellerin et al., 2019).

The overall trend between unmodified Late Devonian seawater and higher $\delta^{34}S_{barite}$ values indicates that barite formed under progressively sulfate limited conditions in which the rate of sulfate depletion exceeds that of sulfate resupply (Torres et al., 1996; Fike et al., 2015). The $\delta^{34}S_{barite}$ values of Brt-2b represent the most evolved isotope signatures (**Figure 12A**), consistent with precipitation under sulfate limitation during later stages of diagenesis (Turchyn and Schrag, 2006; Aller et al., 2010; Gomes and Johnston, 2017). Later changes in the barite front may have resulted in the formation of the vein and pseudomorphic barite (Brt-2c), which formed within pore spaces of existing pyrite and barite (**Figures 7**, **10**) but appears to have precipitated from a similar sulfate pool (**Figure 11**) during the second stage of paragenesis.

Covariation between $\delta^{18}O$ and $\delta^{34}S$ values can provide further information on the diagenetic environment of barite formation. In sediment pore fluids, the slope of the apparent linear phase (SALP; Antler et al., 2013), which describes covariation between $\delta^{18}O$ and $\delta^{34}S$ values, has been linked to sulfate reduction rate (SRR; Böttcher et al., 1998; Böttcher et al., 1999; Aharon and Fu, 2000; Brunner et al., 2005). At low SRR, a high degree of reversibility in the enzymatic pathway of sulfate reduction is thought to promote oxygen isotope exchange between intermediate sulfur phases (e.g., sulfite) and H_2O (Fritz et al., 1989; Brunner and Bernasconi, 2005), resulting in high SALP values. In contrast, where $\delta^{34}S$ values increase without a corresponding increase in $\delta^{18}O$ values (low SALP), it is thought that high SRR results in a lower degree of reversibility (Antler and Pellerin, 2018). At high SRR, kinetic isotope effects will provide the primary control on $\delta^{18}O$ values, resulting in a SALP value of ~0.25 that represents an oxygen fractionation factor that is approximately 25% of sulfur (Mizutani and Rafter, 1973). Importantly, diagenetic mineral phases that contain sulfate (e.g., barite, celestine and carbonates) have the potential to preserve the SALP signature (Antler and Pellerin, 2018). There is a strong positive correlation between $\delta^{18}O$ and $\delta^{34}S$ values in barite from the Canol Formation (**Figure 12B**), which corresponds with a low SALP value and high SRR. Similar low SALP values have been described in authigenic carbonate formed in ancient cold seep environments (e.g., Feng et al., 2016).

Barite Replacement

Barium concentrations in basinal waters are controlled by sulfate concentration and reduction (Torres et al., 2003). The low solubility of barite means the stability field of $BaSO_4$ overlaps with conditions in which reduced sulfur is the dominant sulfur species, rather than sulfate (**Figure 14**). The dissolution and
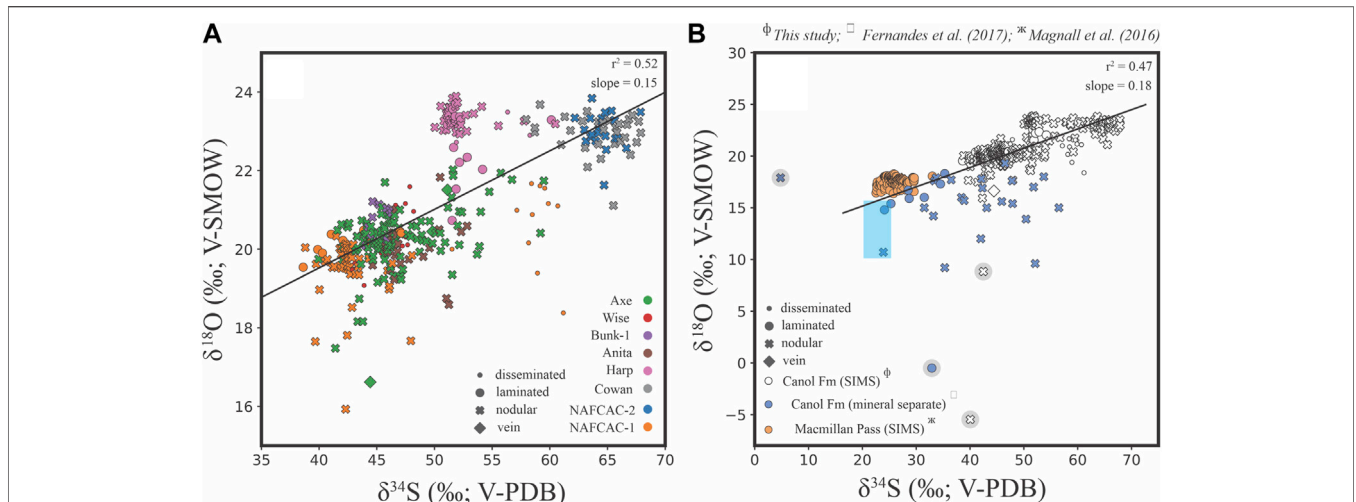
FIGURE 12 | (A) Bivariate plot showing $\delta^{34}S$ values *vs.* $\delta^{18}O$ values generated by SIMS analysis of barite from the Canol Formation. The regression analysis excludes the outliers that are highlighted in **(B)**. **(B)** Bivariate plot showing $\delta^{34}S$ values *vs.* $\delta^{18}O$ values for a compilation of Late Devonian barite data, including mineral separate analyses of Canol Formation barite (Fernandes et al., 2017) and SIMS analyses of barite from Macmillan Pass (Magnall et al., 2016). The regression analysis includes the SIMS and mineral separate data for Canol Formation barite but excludes the outliers from either dataset (highlighted by grey circles). The blue box represents the range of constraints for Late Devonian seawater (John et al., 2010; Chen et al., 2013).
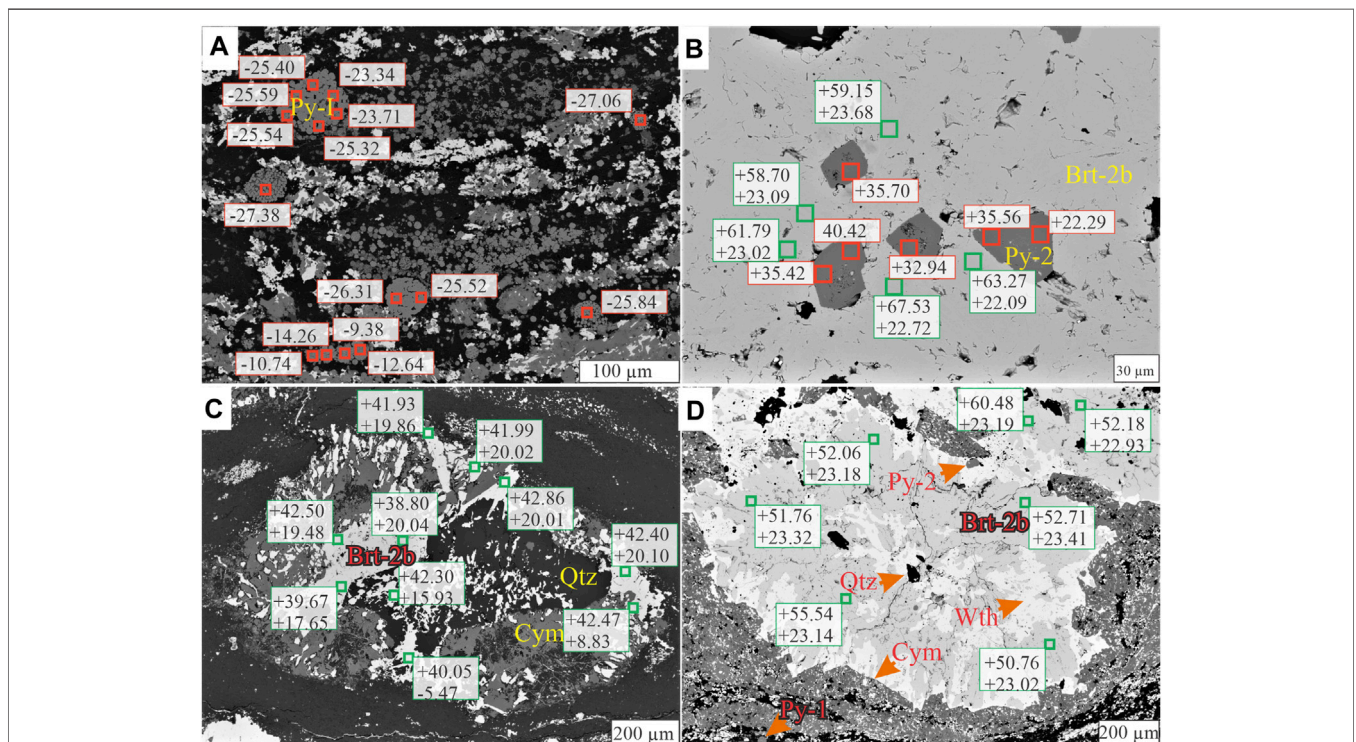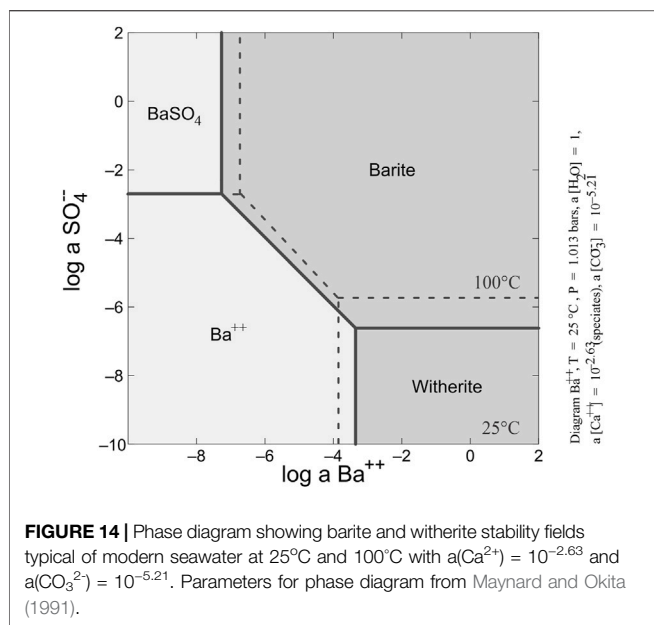

FIGURE 13 | BSE images annotated with pyrite $\delta^{34}S$ values (red squares) and barite $\delta^{34}S$ and $\delta^{18}S$ values (green squares). **(A)** Pyrite framboids and polyframboids (Py-1) in a matrix replaced by cymrite (dark grey) and witherite (white). **(B)** Euhedral pyrite (Py-2) intergrown with Brt-2b. **(C)** Nodular barite ((Brt-2b) replaced by quartz (Qtz) and cymrite (Cym). **(D)** Witherite (Wth) replacement of nodular barite (Brt-2b), both rimmed by cymrite (Cym).

replacement of diagenetic barite may then proceed under conditions of extreme sulfate limitation that typically develop in carbonaceous sediments (Hanor, 2000). The diagenetic barite in the Canol Formation has been replaced by Ba-carbonates (witherite and barytocalcite), followed by Ba-feldspars (hyalophane and cymrite; **Figures 9**, **13D**).

FIGURE 14 | Phase diagram showing barite and witherite stability fields typical of modern seawater at 25°C and 100°C with a(Ca^{2+}) = 10$^{-2.63}$ and a(CO$_3^{2-}$) = 10$^{-5.21}$. Parameters for phase diagram from Maynard and Okita (1991).

The presence of replacive Ba-bearing phases may imply the progressive diagenetic replacement of barite arising from continuous depletion of the sulfate concentration (e.g., Hanor, 2000). High Ba concentrations (around six orders of magnitude relative to seawater) coupled with extreme sulfate depletion have been shown to result in witherite formation (Maynard and Okita (1991). Barium concentrations in modern seawater are between ~5 and 20 μg/L in the open ocean (Hanor, 2000) and up to 60 μg/L occurs in anoxic deep marine environments (Falkner et al., 1993). Thus, Ba concentrations may increase with depth (Paytan and Griffith, 2007; Carter et al., 2020), mediated by microbial activities in the presence of organic matter. Two conditions are suggested by Maynard and Okita (1991) as a prerequisite for witherite replacement of barite; a) a closed or restricted system with sulfate resupply << sulfate reduction; b) high organic matter contents for diagenetic barite conversion to witherite. However, barite dissolution and witherite formation have also been shown as a function of temperature, CO$_2$ dissolution (Busenberg and Plummer, 1986), and pH (Melero-García et al., 2009; Hill et al., 2014), with dissolved carbonate, likely supplied from organic matter degradation (Maynard and Okita, 1991; Hanor, 2000).

Pyrite Formation

Pyrite in the Canol Formation samples preserves end-member δ^{34}S values (**Figure 11**) that are associated with two morphologically distinct stages of pyrite formation (**Figures 13A,B**). Framboidal pyrite (Py-1) in the Canol Formation preserves δ^{34}S values that are significantly lower than Late Devonian seawater (**Figure 11**), which represents a large isotopic fractionation (≤75‰). The δ^{34}S$_{py-2}$ values are more positive (mean = +31.0‰) than upper constraints for Late Devonian seawater (+25‰; John et al., 2010; Chen et al., 2013). The formation of highly positive δ^{34}S$_{pyrite}$ values has been attributed to various processes that include MSR (Drake et al., 2018), sulfide reoxidation (Kah et al., 2016), TSR (Cui et al., 2018; Yan et al., 2020), rapid sedimentation (Pasquier et al., 2017), and sulfate limitation

(Ries et al., 2009). Highly positive δ^{34}S values from mineral separate analyses of pyrite and barite in siliciclastic units from the Selwyn Basin have been interpreted to have developed from water mass restriction and euxinic conditions in the Late Devonian (Goodfellow and Jonasson, 1984). However, the pyrite paragenesis indicates Py-2 precipitated below the SWI during diagenesis (e.g., **Figure 8**) when sulfate limitation would have developed on a much smaller pore fluid scale. Importantly, there is no observable alteration relating to hydrothermal fluids (e.g., Cui et al., 2018; Yan et al., 2020), which rules out any high-temperature origin for Py-2. Highly positive δ^{34}S$_{pyrite}$ values could have developed due to high sedimentation rates reducing the diffusional exchange between diagenetic pore fluids and overlying seawater (e.g., Pasquier et al., 2017). However, there does not appear to be any lithological control on the development of highly positive δ^{34}S$_{pyrite}$ values in the Canol Formation, which may imply that depositional environment was not the primary control on δ^{34}S$_{pyrite}$ values.

The combination of highly positive δ^{34}S$_{pyrite}$ values and evidence of barite solubility represents a trend of progressive sulfate depletion, which is typical of the diagenetic evolution of anoxic sediments (e.g., Torres et al., 1996; Aloisi et al., 2004). Importantly, there is evidence of textural equilibrium between Py-2 and Brt-2 (e.g., **Figure 8**) and it is apparent that δ^{34}S$_{pyrite}$ values do not exceed coeval δ^{34}S$_{barite}$ values (**Figure 11**), meaning they are not strictly "superheavy" (δ^{34}S$_{pyrite}$ > δ^{34}S$_{SO4}$; Ries et al., 2009; Cui et al., 2018). A similar pyrite paragenesis and assemblage between Py-2 and Brt-2 has also been described at Macmillan Pass, where it was linked with two separate stages of diagenetic pyrite formation associated with OSR and AOM-SR (Magnall et al., 2016). Compared to the offset between Py-1 and Late Devonian seawater (Δ^{34}S = 43.3‰), the Δ^{34}S for Brt-2 and Py-2 is smaller (**Figure 11**). This reduced Δ^{34}S value could represent a smaller isotopic fractionation (ε^{34}S), possibly linked with higher SRR that are typical of methane and gas seeps (Deusner et al., 2014). Indeed, the low SALP value that is recorded in barite (**Figure 12A**) would support this interpretation, although it is also possible that Py-2 and Brt-2 did not precipitate precisely at the same time from the same porewater fluids. Nevertheless, the overall evidence of high SRR and increasing sulfate depletion still provides the most plausible explanation for the development of highly positive δ^{34}S$_{pyrite}$ values in the Canol Formation.

Implications

Previous studies on diagenetic pyrite and barite linked highly positive δ^{34}S values to sulfate limitation in a euxinic water column (Goodfellow and Jonasson, 1984). More recent studies have now shown that these isotopic values developed as part of a diagenetic assemblage associated with the SMTZ, where sulfate limitation occurred at the pore fluid scale (e.g., Magnall et al., 2016; Johnson et al., 2018). Notably, the same 2-stage paragenesis comprising framboidal pyrite followed by an assemblage of euhedral pyrite and barite has been identified in Late Devonian strata that host CD-type deposits in the Macmillan Pass district (Magnall et al., 2016). Thus, the formation of highly positive δ^{34}S$_{pyrite}$ values and bedded barite in the Canol Formation is evidence of a similar diagenetic assemblage that has been preserved in unmineralized Late Devonian stratigraphy. Moreover, the preservation of this
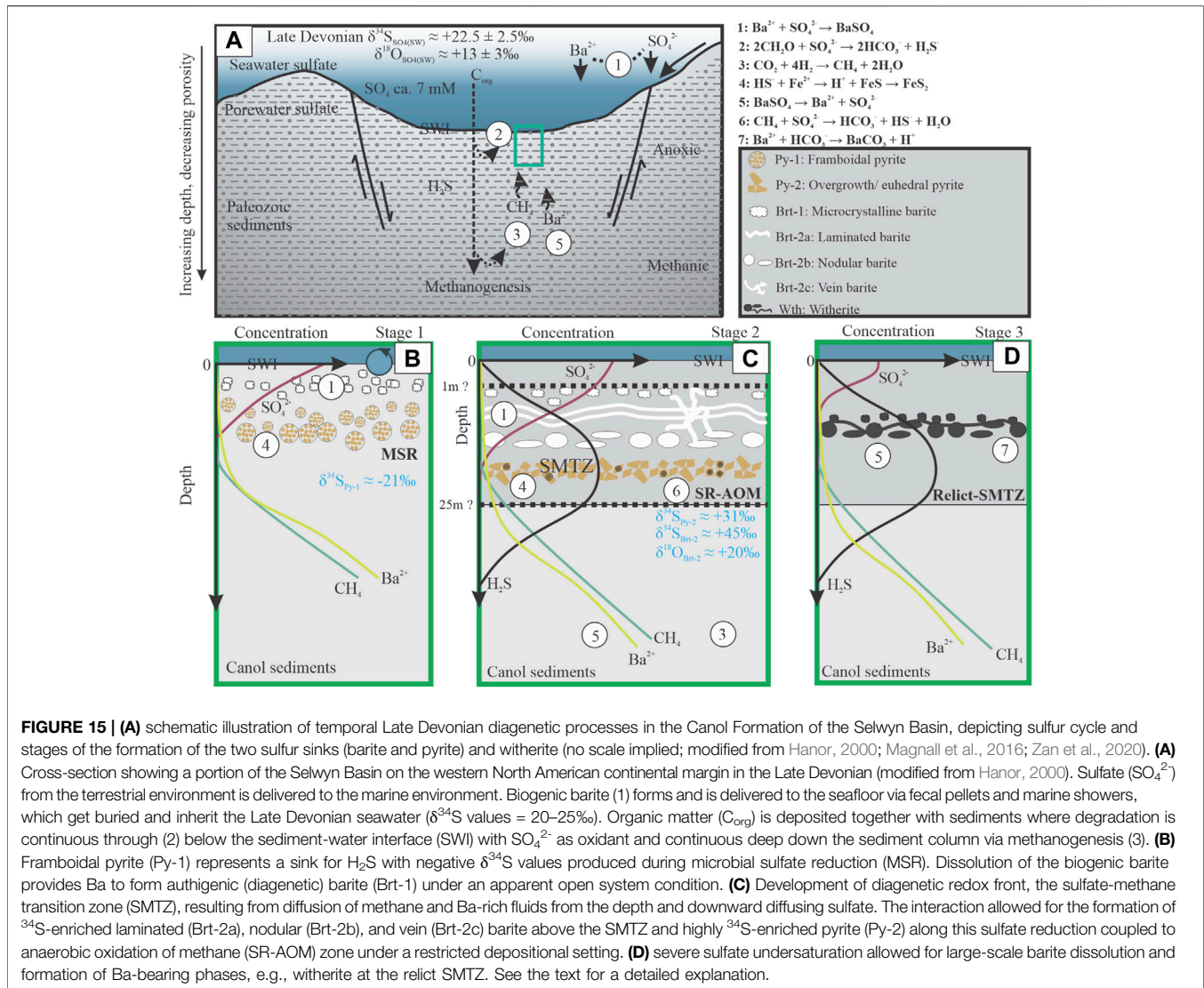
FIGURE 15 | (A) schematic illustration of temporal Late Devonian diagenetic processes in the Canol Formation of the Selwyn Basin, depicting sulfur cycle and stages of the formation of the two sulfur sinks (barite and pyrite) and witherite (no scale implied; modified from Hanor, 2000; Magnall et al., 2016; Zan et al., 2020). **(A)** Cross-section showing a portion of the Selwyn Basin on the western North American continental margin in the Late Devonian (modified from Hanor, 2000). Sulfate (SO_4^{2-}) from the terrestrial environment is delivered to the marine environment. Biogenic barite (1) forms and is delivered to the seafloor via fecal pellets and marine showers, which get buried and inherit the Late Devonian seawater ($\delta^{34}S$ values = 20–25‰). Organic matter (C_{org}) is deposited together with sediments where degradation is continuous through (2) below the sediment-water interface (SWI) with SO_4^{2-} as oxidant and continuous deep down the sediment column via methanogenesis (3). **(B)** Framboidal pyrite (Py-1) represents a sink for H_2S with negative $\delta^{34}S$ values produced during microbial sulfate reduction (MSR). Dissolution of the biogenic barite provides Ba to form authigenic (diagenetic) barite (Brt-1) under an apparent open system condition. **(C)** Development of diagenetic redox front, the sulfate-methane transition zone (SMTZ), resulting from diffusion of methane and Ba-rich fluids from the depth and downward diffusing sulfate. The interaction allowed for the formation of ^{34}S-enriched laminated (Brt-2a), nodular (Brt-2b), and vein (Brt-2c) barite above the SMTZ and highly ^{34}S-enriched pyrite (Py-2) along this sulfate reduction coupled to anaerobic oxidation of methane (SR-AOM) zone under a restricted depositional setting. **(D)** severe sulfate undersaturation allowed for large-scale barite dissolution and formation of Ba-bearing phases, e.g., witherite at the relict SMTZ. See the text for a detailed explanation.

assemblage in multiple stratigraphic sections in the Canol Formation implies periodical stability in the SMTZ on a large scale (> 10 km) in order to allow pyrite and barite to accumulate (e.g., Lin et al., 2017; Liu et al., 2019).

In the modern oceans, shallow SMTZ and high methane fluxes are located along productive continental margins with high sedimentation rates (Egger et al., 2018). Other factors controlling the depth of the SMTZ include organic matter content and decomposition and sulfate concentrations (Torres et al., 2003; Jørgensen et al., 2004; Borowski et al., 2013; Lin et al., 2016; Lin et al., 2017; Liu et al., 2019; Liu et al., 2020; Liu et al., 2021). In the Canol Formation, high total organic carbon (1.5–9.2 wt%; Kabanov and Gouwy, 2017) is associated with facies characterized by dynamic sedimentation, in which bioturbation has been linked with partial oxygenation (Biddle et al., 2021). The stabilization of the SMTZ is likely to have required constant fluxes of methane and sulfate coupled with a hiatus in sedimentation, and changes to any of these parameters could potentially have resulted in the alteration of authigenic mineral phases (Arning et al., 2015). The relatively

minor replacement of Py-2 by veined Brt-2c (**Figure 10**) may therefore suggest abrupt albeit short-lived fluctuation of the SMTZ due to changes in either methane or sulfate fluxes within the sediments. Barite solubility is drastically increased below the SMTZ, and where sulfate concentrations diminish, Ba diffuses upward and reacts with other available cations (Maynard and Okita, 1991; Hanor, 2000). Considering that SR-AOM in the SMTZ also leads to the generation of alkalinity, this may explain the origin of barium carbonate in these samples (e.g., **Figure 13D**). The origin of carbonate in these samples could be evaluated using carbon isotopes, but this is beyond the scope of this study.

Similar barite-pyrite-Ba-carbonate/silicate assemblages have also been reported in other Paleozoic strata (e.g., Maynard and Okita, 1991; Jewell, 2000; Koski and Hein, 2004), including Qinling-Daba region, southern China (Wang and Li, 1991; Xu et al., 2016). The low seawater concentrations in the Lower Paleozoic (ca. <1–10 mM; Horita et al., 2002; Brennan et al., 2004; Gill et al., 2007), relative to modern ocean seawater sulfate that is about 28 mM (Rickard, 2012; Fike et al., 2015; Jorgensen

et al., 2019), would have restricted the amount of sulfate resupply below the seafloor in organic-rich sediments (Greinert et al., 2002; Paytan et al., 2002). Continuous fractionation of the porewater sulfate through OSR and SR-AOM likely led to the formation of highly positive $\delta^{34}S_{pyrite}$ values in this study and other similar settings. We would suggest that highly positive $\delta^{34}S_{pyrite}$ values and barite formation, dissolution, and replacement by other Ba-bearing phases might have been a more general feature of methane diagenesis in the lower Paleozoic.

CONCLUSION

The diagenetic sulfur cycle in the Selwyn Basin has been reconstructed using microscale (SIMS) paired isotope constraints on pyrite and barite in samples from multiple stratigraphic sections of Late Devonian sedimentary rocks. Two distinct stages of pyrite formation formed via microbial sulfate reduction (MSR) under contrasting levels of sulfate availability. The initial stage of pyrite formation developed during early diagenesis under relatively open-system conditions, which resulted in the precipitation of the framboidal pyrite (Py-1) and preservation of negative $\delta^{34}S$ values. Deeper in the sediment profile, MSR resulted in progressive sulfate depletion and the development of the sulfate methane transition zone (SMTZ), where sulfate reduction was coupled with the anaerobic oxidation of methane (SR-AOM). Highly positive $\delta^{34}S$ values in pyrite developed as a result of high sulfate reduction rates and progressive depletion of sulfate. Sulfate limited, methane-rich diagenetic fluids beneath the SMTZ provided conditions under which barium was soluble. Barite formed when opposing diffusional fluxes of barium and sulfate bearing fluids mixed at the SMTZ. Importantly, the paragenetically constrained analyses indicate that highly positive $\delta^{34}S_{pyrite}$ values formed during diagenesis in multiple correlated stratigraphic sections from the Late Devonian in the Selwyn Basin, indicating this diagenetic assemblage was a regional feature. We propose that the formation of highly positive $\delta^{34}S$ values in pyrite, dissolution of barite, and replacement by other Ba-bearing phases, could have been a more general features of methane diagenesis in the lower Paleozoic.

DATA AVAILABILITY STATEMENT

AUTHOR CONTRIBUTIONS

SG and JM designed the study. HG prepared the samples and performed the petrographic analysis (optical microscopy, EPMA-EDS, and SEM). MW conducted the SIMS analyses in coordination with HG and JM. HG interpreted the data and wrote the manuscript with contributions from JM, SG, H-MS, and MW.

FUNDING

ACKNOWLEDGMENTS

REFERENCES

Aharon, P., and Fu, B. (2000). Microbial Sulfate Reduction Rates and Sulfur and Oxygen Isotope Fractionations at Oil and Gas Seeps in deepwater Gulf of Mexico. *Geochim. et Cosmochim. Acta* 64 (2), 233–246. doi:10.1016/s0016-7037(99)00292-6

Aller, R. C., Madrid, V., Chistoserdov, A., Aller, J. Y., and Heilbrun, C. (2010). Unsteady Diagenetic Processes and Sulfur Biogeochemistry in Tropical Deltaic Muds: Implications for Oceanic Isotope Cycles and the Sedimentary Record. *Geochim. Cosmochim. Acta* 74 (16), 4671–4692. doi:10.1016/j.gca.2010.05.008

Aloisi, G., Wallmann, K., Bollwerk, S. M., Derkachev, A., Bohrmann, G., and Suess, E. (2004). The Effect of Dissolved Barium on Biogeochemical Processes at Cold Seeps. *Geochim. Cosmochim. Acta* 68 (8), 1735–1748. doi:10.1016/j.gca.2003.10.010

Antler, G., and Pellerin, A. (2018). A Critical Look at the Combined Use of Sulfur and Oxygen Isotopes to Study Microbial Metabolisms in Methane-Rich Environments. *Front. Microbiol.* 9, 519. doi:10.3389/fmicb.2018.00519

Antler, G., Turchyn, A. V., Rennie, V., Herut, B., and Sivan, O. (2013). Coupled Sulfur and Oxygen Isotope Insight into Bacterial Sulfate Reduction in the Natural Environment. *Geochim. Cosmochim. Acta* 118, 98–117. doi:10.1016/j.gca.2013.05.005

Aplin, A. C., and Macquaker, J. H. S. (2011). Mudstone Diversity: Origin and Implications for Source, Seal, and Reservoir Properties in Petroleum Systems. *Bulletin* 95 (12), 2031–2059. doi:10.1306/03281110162

Arning, E. T., Gaucher, E. C., van Berk, W., and Schulz, H.-M. (2015). Hydrogeochemical Models Locating Sulfate-Methane Transition Zone in marine Sediments Overlying Black Shales: A New Tool to Locate Biogenic Methane? *Mar. Pet. Geol.* 59, 563–574. doi:10.1016/j.marpetgeo.2014.10.004

Barnes, R. O., and Goldberg, E. D. (1976). Methane Production and Consumption in Anoxic marine Sediments. *Geol* 4 (5), 297–300. doi:10.1130/0091-7613(1976)4<297:mpacia>2.0.co;2

Biddle, S. K., LaGrange, M. T., Harris, B. S., Fiess, K., Terlaky, V., and Gingras, M. K. (2021). A fine Detail Physico-Chemical Depositional Model for Devonian Organic-Rich Mudstones: A Petrographic Study of the Hare Indian and Canol

Formations, Central Mackenzie Valley, Northwest Territories. *Sediment. Geol.* 414, 105838. doi:10.1016/j.sedgeo.2020.105838

Böttcher, M. E., Oelschläger, B., Höpner, T., Brumsack, H.-J., and Rullkötter, J. (1998). Sulfate Reduction Related to the Early Diagenetic Degradation of Organic Matter and "Black Spot" Formation in Tidal Sandflats of the German Wadden Sea (Southern North Sea): Stable Isotope (13C, 34S, 18O) and Other Geochemical Results. *Org. Geochem.* 29 (5-7), 1517–1530. doi:10.1016/s0146-6380(98)00124-7

Böttcher, M. E., Sievert, S. M., and Kuever, J. (1999). Fractionation of Sulfur Isotopes during Dissimilatory Reduction of Sulfate by a Thermophilic Gram-Negative Bacterium at 60 C. *Arch. Microbiol.* 172 (2), 125–128. doi:10.1007/s002030050749

Borowski, W. S., Rodriguez, N. M., Paull, C. K., and Ussler, W. (2013). Are 34S-Enriched Authigenic Sulfide Minerals a Proxy for Elevated Methane Flux and Gas Hydrates in the Geologic Record? *Mar. Pet. Geol.* 43, 381–395. doi:10.1016/j.marpetgeo.2012.12.009

Bottrell, S. H., and Newton, R. J. (2006). Reconstruction of Changes in Global Sulfur Cycling from marine Sulfate Isotopes. *Earth-Science Rev.* 75 (1-4), 59–83. doi:10.1016/j.earscirev.2005.10.004

Brennan, S. T., Lowenstein, T. K., and Horita, J. (2004). Seawater Chemistry and the Advent of Biocalcification. *Geol* 32 (6), 473–476. doi:10.1130/g20251.1

Brunner, B., and Bernasconi, S. M. (2005). A Revised Isotope Fractionation Model for Dissimilatory Sulfate Reduction in Sulfate Reducing Bacteria. *Geochim. Cosmochim. Acta* 69 (20), 4759–4771. doi:10.1016/j.gca.2005.04.015

Brunner, B., Bernasconi, S. M., Kleikemper, J., and Schroth, M. H. (2005). A Model for Oxygen and Sulfur Isotope Fractionation in Sulfate during Bacterial Sulfate Reduction Processes. *Geochim. Cosmochim. Acta* 69 (20), 4773–4785. doi:10.1016/j.gca.2005.04.017

Bryant, R. N., Jones, C., Raven, M. R., Gomes, M. L., Berelson, W. M., Bradley, A. S., et al. (2019). Sulfur Isotope Analysis of Microcrystalline Iron Sulfides Using Secondary Ion Mass Spectrometry Imaging: Extracting Local Paleo-Environmental Information from Modern and Ancient Sediments. *Rapid Commun. Mass. Spectrom.* 33 (5), 491–502. doi:10.1002/rcm.8375

Bryant, R. N., Jones, C., Raven, M. R., Owens, J. D., and Fike, D. A. (2020). Shifting Modes of Iron Sulfidization at the Onset of OAE-2 Drive Regional Shifts in Pyrite δ34S Records. *Chem. Geol.* 553, 119808. doi:10.1016/j.chemgeo.2020.119808

Busenberg, E., and Plummer, L. N. (1986). The Solubility of BaCO3(cr) (Witherite) in CO2-H2O Solutions between 0 and 90°C, Evaluation of the Association Constants of BaHCO3+(aq) and BaCO30(aq) between 5 and 80°C, and a Preliminary Evaluation of the Thermodynamic Properties of Ba2+(aq). *Geochim. Cosmochim. Acta* 50 (10), 2225–2233. doi:10.1016/0016-7037(86)90077-3

Canet, C., Anadón, P., González-Partida, E., Alfonso, P., Rajabi, A., Pérez-Segura, E., et al. (2014). Paleozoic Bedded Barite Deposits from Sonora (NW Mexico): Evidence for a Hydrocarbon Seep Environment of Formation. *Ore Geol. Rev.* 56, 292–300. doi:10.1016/j.oregeorev.2013.06.009

Canfield, D. E., Farquhar, J., and Zerkle, A. L. (2010). High Isotope Fractionations during Sulfate Reduction in a Low-Sulfate Euxinic Ocean Analog. *Geology* 38 (5), 415–418. doi:10.1130/G30723.1

Canfield, D. E. (2001a). 12. Biogeochemistry of Sulfur Isotopes. *Stable Isotope Geochem.* 43(1), 607–636. doi:10.1515/9781501508745-015

Canfield, D. E. (2001b). Isotope Fractionation by Natural Populations of Sulfate-Reducing Bacteria. *Geochim. Cosmochim. Acta* 65(7), 1117–1124. doi:10.1016/S0016-7037(00)00584-6

Carter, S. C., Paytan, A., and Griffith, E. M. (2020). Toward an Improved Understanding of the Marine Barium Cycle and the Application of Marine Barite as a Paleoproductivity Proxy. *Minerals* 10 (5), 421. doi:10.3390/min10050421

Cecile, M. P., Shakur, M. A., and Krouse, H. R. (1983). The Isotopic Composition of Western Canadian Barites and the Possible Derivation of Oceanic Sulphate δ34S and δ18O Age Curves. *Can. J. Earth Sci.* 20 (10), 1528–1535. doi:10.1139/e83-142

Chen, D., Wang, J., Racki, G., Li, H., Wang, C., Ma, X., et al. (2013). Large sulphur Isotopic Perturbations and Oceanic Changes during the Frasnian-Famennian Transition of the Late Devonian. *J. Geol. Soc.* 170 (3), 465–476. doi:10.1144/jgs2012-037

Clark, I. D., Ilin, D., Jackson, R. E., Jensen, M., Kennell, L., Mohammadzadeh, H., et al. (2015). Paleozoic-aged Microbial Methane

in an Ordovician Shale and Carbonate Aquiclude of the Michigan Basin, Southwestern Ontario. *Org. Geochem.* 83-84, 118–126. doi:10.1016/j.orggeochem.2015.03.006

Cui, H., Kitajima, K., Spicuzza, M. J., Fournelle, J. H., Denny, A., Ishida, A., et al. (2018). Questioning the Biogenicity of Neoproterozoic Superheavy Pyrite by SIMS. *Am. Mineral.* 103 (9), 1362–1400. doi:10.2138/am-2018-6489

Deusner, C., Holler, T., Arnold, G. L., Bernasconi, S. M., Formolo, M. J., and Brunner, B. (2014). Sulfur and Oxygen Isotope Fractionation during Sulfate Reduction Coupled to Anaerobic Oxidation of Methane Is Dependent on Methane Concentration. *Earth Planet. Sci. Lett.* 399, 61–73. doi:10.1016/j.epsl.2014.04.047

Dickens, G. R., O'Neil, J. R., Rea, D. K., and Owen, R. M. (1995). Dissociation of Oceanic Methane Hydrate as a Cause of the Carbon Isotope Excursion at the End of the Paleocene. *Paleoceanography* 10 (6), 965–971. doi:10.1029/95pa02087

Dickens, G. R. (2001). Sulfate Profiles and Barium Fronts in Sediment on the Blake Ridge: Present and Past Methane Fluxes through a Large Gas Hydrate Reservoir. *Geochim. Cosmochim. Acta* 65(4), 529–543. doi:10.1016/S0016-7037(00)00556-1

Drake, H., Whitehouse, M. J., Heim, C., Reiners, P. W., Tillberg, M., Hogmalm, K. J., et al. (2018). Unprecedented 34 S-enrichment of Pyrite Formed Following Microbial Sulfate Reduction in Fractured Crystalline Rocks. *Geobiology* 16 (5), 556–574. doi:10.1111/gbi.12297

Egger, M., Riedinger, N., Mogollón, J. M., and Jørgensen, B. B. (2018). Global Diffusive Fluxes of Methane in marine Sediments. *Nat. Geosci.* 11 (6), 421–425. doi:10.1038/s41561-018-0122-8

Falkner, K. K., Klinkhammer, G. P., Bowers, T. S., Todd, J. F., Lewis, B. L., Landing, W. M., et al. (1993). The Behavior of Barium in Anoxic Marine Waters. *Geochim. Cosmochim. Acta* 57(3), 537–554. doi:10.1016/0016-7037(93)90366-5

Farquhar, J., Wu, N., Canfield, D. E., and Oduro, H. (2010). Connections between Sulfur Cycle Evolution, Sulfur Isotopes, Sediments, and Base Metal Sulfide Deposits. *Econ. Geology.* 105(3), 509–533. doi:10.2113/gsecongeo.105.3.509

Feng, D., Peng, Y., Bao, H., Peckmann, J., Roberts, H. H., and Chen, D. (2016). A Carbonate-Based Proxy for Sulfate-Driven Anaerobic Oxidation of Methane. *Geology* 44 (12), 999–1002. doi:10.1130/g38233.1

Fernandes, N. A., Gleeson, S. A., Magnall, J. M., Creaser, R. A., Martel, E., Fischer, B. J., et al. (2017). The Origin of Late Devonian (Frasnian) Stratiform and Stratabound Mudstone-Hosted Barite in the Selwyn Basin, Northwest Territories, Canada. *Mar. Pet. Geol.* 85, 1–15. doi:10.1016/j.marpetgeo.2017.04.006

Fernandes, N. (2011). *Geology and Geochemistry of Late Devonian-Mississipian Sediment-Hosted Barite Sequences of the Selwyn Basin, NWT and Yukon, Canada*. MSc thesis. Edmonton, Alberta: University of Alberta.

Fike, D. A., Bradley, A. S., and Rose, C. V. (2015). Rethinking the Ancient Sulfur Cycle. *Annu. Rev. Earth Planet. Sci.* 4343 (1), 593–622. doi:10.1146/annurev-earth-060313-054802

Fritz, P., Basharmal, G. M., Drimmie, R. J., Ibsen, J., and Qureshi, R. M. (1989). Oxygen Isotope Exchange between Sulphate and Water during Bacterial Reduction of Sulphate. *Chem. Geol. Isotope Geosci. Sect.* 79 (2), 99–105. doi:10.1016/0168-9622(89)90012-2

Gadd, M. G., Layton-Matthews, D., and Peter, J. M. (2016). Non-Hydrothermal Origin of Apatite in SEDEX Mineralization and Host Rocks of the Howard's Pass District, Yukon, Canada. *Am. Mineral.* 101 (5-6), 1061–1071. doi:10.2138/am-2016-5550

Gill, B. C., Lyons, T. W., and Saltzman, M. R. (2007). Parallel, High-Resolution Carbon and Sulfur Isotope Records of the Evolving Paleozoic marine Sulfur Reservoir. *Palaeogeogr. Palaeoclimatol. Palaeoecol.* 256 (3-4), 156–173. doi:10.1016/j.palaeo.2007.02.030

Goldberg, T., Mazumdar, A., Strauss, H., and Shields, G. (2006). Insights from Stable S and O Isotopes into Biogeochemical Processes and Genesis of Lower Cambrian Barite-Pyrite Concretions of South China. *Org. Geochem.* 37 (10), 1278–1288. doi:10.1016/j.orggeochem.2006.04.013

Gomes, M. L., and Johnston, D. T. (2017). Oxygen and Sulfur Isotopes in Sulfate in Modern Euxinic Systems with Implications for Evaluating the Extent of Euxinia in Ancient Oceans. *Geochim. Cosmochim. Acta* 205, 331–359. doi:10.1016/j.gca.2017.02.020

Gonzalez-Muñoz, M., Martinez-Ruiz, F., Morcillo, F., Martin-Ramos, J., and Paytan, A. (2012). Precipitation of Barite by marine Bacteria: A Possible Mechanism for marine Barite Formation. *Geology* 40 (8), 675–678. doi:10.1130/g33006.1

Goodfellow, W. D., and Jonasson, I. R. (1984). Ocean Stagnation and Ventilation Defined by δ34S Secular Trends in Pyrite and Barite, Selwyn Basin, Yukon. *Geol* 12 (10), 583–586. doi:10.1130/0091-7613(1984)12<583:osavdb>2.0.co;2

Goodfellow, W., and Lydon, J. (2007). "Sedimentary Exhalative (SEDEX) Deposits," in *Mineral Deposits of Canada: A Synthesis of Major deposit Types, District Metallogeny, the Evolution of Geological Provinces, and Exploration Methods* (Geological Association of Canada, Mineral Deposits Division, Special Publication), 5, 163–183.

Goodfellow, W. D. (1987). Anoxic Stratified Oceans as a Source of sulphur in Sediment-Hosted Stratiform ZnPb Deposits (Selwyn Basin, Yukon, Canada). *Chem. Geol. Isotope Geosci. Sect.* 65 (3-4), 359–382. doi:10.1016/0168-9622(87)90014-5

Gordey, S. P. (1993). Evolution of the Northern Cordilleran Miogeocline, Nahanni Map Area (105I), Yukon and Northwest Territories. *Geol. Surv. Can. Mem.* 428, 214. doi:10.4095/183983

Gordey, S. P. (2013). Evolution of the Selwyn Basin Region, Sheldon Lake and Tay River Map Areas, Central Yukon. *Geol. Surv. Can. Bull.* 599, 176. doi:10.4095/293034

Greinert, J., Bollwerk, S. M., Derkachev, A., Bohrmann, G., and Suess, E. (2002). Massive Barite Deposits and Carbonate Mineralization in the Derugin Basin, Sea of Okhotsk: Precipitation Processes at Cold Seep Sites. *Earth Planet. Sci. Lett.* 203 (1), 165–180. doi:10.1016/S0012-821x(02)00830-0

Grema, H. M., Magnall, J. M., Whitehouse, M. J., Gleeson, S. A., and Schulz, H.-M. (2021). Isotopic Data of Pyrite (δ34S) and Barite (δ34S, δ18O) in the Canol Formation (Selwyn Basin, Canada). *GFZ Data Services*. doi:10.5880/GFZ.3.1.2021.006

Griffith, E. M., and Paytan, A. (2012). Barite in the Ocean - Occurrence, Geochemistry and Palaeoceanographic Applications. *Sedimentology* 59 (6), 1817–1835. doi:10.1111/j.1365-3091.2012.01327.x

Hanor, J. S. (2000). Barite-celestine Geochemistry and Environments of Formation. *Sulfate Minerals - Crystallogr. Geochem. Environ. Signif.* 40(1), 193–275. doi:10.2138/rmg.2000.40.4

Hill, P. S., Tripati, A. K., and Schauble, E. A. (2014). Theoretical Constraints on the Effects of pH, Salinity, and Temperature on Clumped Isotope Signatures of Dissolved Inorganic Carbon Species and Precipitating Carbonate Minerals. *Geochim. Cosmochim. Acta* 125, 610–652. doi:10.1016/j.gca.2013.06.018

Horita, J., Zimmermann, H., and Holland, H. D. (2002). Chemical Evolution of Seawater during the Phanerozoic. *Geochim. Cosmochim. Acta* 66 (21), 3733–3756. doi:10.1016/S0016-7037(01)00884-5

Jewell, P. W. (2000). "Bedded Barite in the Geologic Record," in *Marine Authigenesis: From Global to Microbial: SEPM*. Editors C. R. Glenn, L. Prévôt-Lucas, and J. Lucas (Tulsa, Oklahoma: Society for Sedimentary Geology, Special Publication), 66, 147–161. doi:10.2110/pec.00.66.0147

Jørgensen, B. B., and Kasten, S. (2006). "Sulfur Cycling and Methane Oxidation," in *Marine Geochemistry* (Springer), 271–309.

Jørgensen, B. B., Böttcher, M. E., Lüschen, H., Neretin, L. N., and Volkov, I. I. (2004). Anaerobic Methane Oxidation and a Deep H2S Sink Generate Isotopically Heavy Sulfides in Black Sea Sediments. *Geochim. Cosmochim. Acta* 68 (9), 2095–2118. doi:10.1016/j.gca.2003.07.017

John, E. H., Wignall, P. B., Newton, R. J., and Bottrell, S. H. (2010). δ34SCAS and δ18OCAS Records during the Frasnian–Famennian (Late Devonian) Transition and Their Bearing on Mass Extinction Models. *Chem. Geol.* 275 (3-4), 221–234. doi:10.1016/j.chemgeo.2010.05.012

Johnson, C. A., Emsbo, P., Poole, F. G., and Rye, R. O. (2009). Sulfur- and Oxygen-Isotopes in Sediment-Hosted Stratiform Barite Deposits. *Geochim. Cosmochim. Acta* 73 (1), 133–147. doi:10.1016/j.gca.2008.10.011

Johnson, C. A., Slack, J. F., Dumoulin, J. A., Kelley, K. D., and Falck, H. (2018). Sulfur Isotopes of Host Strata for Howards Pass (Yukon-Northwest Territories) Zn-Pb Deposits Implicate Anaerobic Oxidation of Methane, Not basin Stagnation. *Geology* 46 (7), 619–622. doi:10.1130/g40274.1

Jørgensen, B. B., Findlay, A. J., and Pellerin, A. (2019). The Biogeochemical Sulfur Cycle of Marine Sediments. *Front. Microbiol.* 10, 849. doi:10.3389/fmicb.2019.00849

Kabanov, P., and Gouwy, S. A. (2017). The Devonian Horn River Group and the Basal Imperial Formation of the central Mackenzie Plain, N.W.T., Canada: Multiproxy Stratigraphic Framework of a Black Shale basin. *Can. J. Earth Sci.* 54 (4), 409–429. doi:10.1139/cjes-2016-0096

Kah, L. C., Lyons, T. W., and Frank, T. D. (2004). Low marine Sulphate and Protracted Oxygenation of the Proterozoic Biosphere. *Nature* 431 (7010), 834–838. doi:10.1038/nature02974

Kah, L. C., Thompson, C. K., Henderson, M. A., and Zhan, R. (2016). Behavior of marine Sulfur in the Ordovician. *Palaeogeogr. Palaeoclimatol. Palaeoecol.* 458, 133–153. doi:10.1016/j.palaeo.2015.12.028

Kaplan, I. R., and Rittenberg, S. C. (1964). Microbiological Fractionation of Sulphur Isotopes. *J. Gen. Microbiol.* 34 (2), 195–212. doi:10.1099/00221287-34-2-195

Klemme, H., and Ulmishek, G. F. (1991). Effective Petroleum Source Rocks of the World: Stratigraphic Distribution and Controlling Depositional Factors. *AAPG Bull.* 75 (12), 1809–1851. doi:10.1306/0c9b2a47-1710-11d7-8645000102c1865d

Knittel, K., and Boetius, A. (2009). Anaerobic Oxidation of Methane: Progress with an Unknown Process. *Annu. Rev. Microbiol.* 63, 311–334. doi:10.1146/annurev.micro.61.080706.093130

Koski, R. A., and Hein, J. R. (2004). *Stratiform Barite Deposits in the Roberts Mountains Allochthon, Nevada: A Review of Potential Analogs in Modern Sea-Floor Environments: U.S. Geological Survey Bulletin 2209–H,* 17.

Large, R. R., Bull, S. W., McGoldrick, P. J., and Walters, S. (2005). Stratiform and Strata-Bound Zn-Pb-Ag Deposits in Proterozoic Sedimentary Basins, Northern Australia. *Econ. Geol.* 100, 931–963. doi:10.5382/av100.28

Leach, D., Marsh, E., Bradley, D., Gardoll, S., and Huston, D. (2005). "The Distribution of SEDEX Pb-Zn Deposits through Earth History," in *Mineral Deposit Research: Meeting the Global Challenge*. doi:10.1007/3-540-27946-6_38

Leach, D. L., Bradley, D. C., Huston, D., Pisarevsky, S. A., Taylor, R. D., and Gardoll, S. J. (2010). Sediment-Hosted Lead-Zinc Deposits in Earth History. *Econ. Geol.* 105(3), 593–625. doi:10.2113/gsecongeo.105.3.593

Lin, Z., Sun, X., Peckmann, J., Lu, Y., Xu, L., Strauss, H., et al. (2016). How Sulfate-Driven Anaerobic Oxidation of Methane Affects the Sulfur Isotopic Composition of Pyrite: A SIMS Study from the South China Sea. *Chem. Geol.* 440, 26–41. doi:10.1016/j.chemgeo.2016.07.007

Lin, Z., Sun, X., Strauss, H., Lu, Y., Gong, J., Xu, L., et al. (2017). Multiple Sulfur Isotope Constraints on Sulfate-Driven Anaerobic Oxidation of Methane: Evidence from Authigenic Pyrite in Seepage Areas of the South China Sea. *Geochim. Cosmochim. Acta* 211, 153–173. doi:10.1016/j.gca.2017.05.015

Liseroudi, M. H., Ardakani, O. H., Pedersen, P. K., Stern, R. A., Wood, J. M., and Sanei, H. (2021). Microbial and Thermochemical Controlled Sulfur Cycle in the Early Triassic Sediments of the Western Canadian Sedimentary Basin. *J. Geol. Soc.* 178 (4). doi:10.1144/jgs2020-175

Liu, X., Fike, D., Li, A., Dong, J., Xu, F., Zhuang, G., et al. (2019). Pyrite Sulfur Isotopes Constrained by Sedimentation Rates: Evidence from Sediments on the East China Sea Inner Shelf since the Late Pleistocene. *Chem. Geology.* 505, 66–75. doi:10.1016/j.chemgeo.2018.12.014

Liu, J., Pellerin, A., Izon, G., Wang, J., Antler, G., Liang, J., et al. (2020). The Multiple sulphur Isotope Fingerprint of a Sub-seafloor Oxidative sulphur Cycle Driven by Iron. *Earth Planet. Sci. Lett.* 536, 116165. doi:10.1016/j.epsl.2020.116165

Liu, J., Pellerin, A., Wang, J., Rickard, D., Antler, G., Zhao, J., et al. (2021). Multiple sulphur Isotopes Discriminate Organoclastic and Methane-Based Sulfate Reduction by Sub-Seafloor Pyrite Formation. *Geochim. Cosmochim. Acta* 316, 309–330. doi:10.1016/j.gca.2021.09.026

Machel, H. G. (2001). Bacterial and Thermochemical Sulfate Reduction in Diagenetic Settings - Old and New Insights. *Sediment. Geol.* 140(1-2), 143–175. doi:10.1016/S0037-0738(00)00176-7

Magnall, J. M., Gleeson, S. A., Stern, R. A., Newton, R. J., Poulton, S. W., and Paradis, S. (2016). Open System Sulphate Reduction in a Diagenetic Environment - Isotopic Analysis of Barite (δ34S and δ18O) and Pyrite (δ34S) from the Tom and Jason Late Devonian Zn-Pb-Ba Deposits, Selwyn Basin, Canada. *Geochim. Cosmochim. Acta* 180, 146–163. doi:10.1016/j.gca.2016.02.015

Magnall, J. M., Gleeson, S. A., Hayward, N., and Rocholl, A. (2020a). Massive Sulfide Zn Deposits in the Proterozoic Did Not Require Euxinia. *Geochem. Persp. Let.*, 19–24. doi:10.7185/geochemlet.2008

Magnall, J. M., Gleeson, S. A., and Paradis, S. (2020b). A New Subseafloor Replacement Model for the Macmillan Pass Clastic-Dominant Zn-Pb ± Ba Deposits (Yukon, Canada). *Econ. Geology.* 115 (5), 953–959. doi:10.5382/econgeo.4719

Mair, J. L., Hart, C. J. R., and Stephens, J. R. (2006). Deformation History of the Northwestern Selwyn Basin, Yukon, Canada: Implications for Orogen Evolution and Mid-Cretaceous Magmatism. *Geol. Soc. Am. Bull.* 118 (3-4), 304–323. doi:10.1130/B25763.1

Marin-Carbonne, J., Remusat, L., Sforna, M. C., Thomazo, C., Cartigny, P., and Philippot, P. (2018). Sulfur Isotope's Signal of Nanopyrites Enclosed in 2.7 Ga Stromatolitic Organic Remains Reveal Microbial Sulfate Reduction. *Geobiology* 16 (2), 121–138. doi:10.1111/gbi.12275

Martel, E., Turner, E., and Fischer, B. (2011). *Geology of the central Mackenzie Mountains of the Northern Canadian Cordillera, Sekwi Mountain (105P), Mount Eduni (106A), and Northwestern Wrigley Lake (95M) Map-Areas, Northwest Territories*, 1. Yellowknife: Northwest Territories Geoscience Office, NWT Special, 423.

Martínez Ruíz, F. C., Paytan, A., González Muñoz, M. T., Jroundi, F., Abad, M. d. M., Lam, P. J., et al. (2020). Barite Precipitation on Suspended Organic Matter in the Mesopelagic Zone. *Front. Earth. Sci.* 8, 567714. doi:10.3389/feart.2020.567714

Maynard, J. B., and Okita, P. M. (1991). Bedded Barite Deposits in the United States, Canada, Germany, and China; Two Major Types Based on Tectonic Setting. *Econ. Geol. Bull. Soc. Econ. Geol.* 86(2), 364–376. doi:10.2113/gsecongeo.86.2.364

Melero-García, E., Santisteban-Bailón, R., and García-Ruiz, J. (2009). Role of Bulk pH during Witherite Biomorph Growth in Silica Gels. *Cryst. Growth Des.* 9 (11), 4730–4734. doi:10.1021/cg9005967

Mizutani, Y., and Rafter, T. A. (1973). Isotopic Behaviour of Sulphate Oxygen in the Bacterial Reduction of Sulphate. *Geochem. J.* 6 (4), 183–191. doi:10.2343/geochemj.6.183

Morrow, D. W. (2018). Devonian of the Northern Canadian Mainland Sedimentary Basin: A Review. *Bull. Can. Petrol. Geol.* 66 (3), 623–694–

Ootes, L., Gleeson, S. A., Turner, E., Rasmussen, K., Gordey, S., Falck, H., et al. (2013). Metallogenic Evolution of the Mackenzie and Eastern Selwyn Mountains of Canada's Northern Cordillera, Northwest Territories: A Compilation and Review. *Gs* 40 (1), 40–69. doi:10.12789/geocanj.2013.40.005

Pasquier, V., Sansjofre, P., Rabineau, M., Revillon, S., Houghton, J., and Fike, D. A. (2017). Pyrite Sulfur Isotopes Reveal Glacial–interglacial Environmental Changes. *Proc. Natl. Acad. Sci. USA* 114 (23), 5941–5945. doi:10.1073/pnas.1618245114

Pasquier, V., Bryant, R. N., Fike, D. A., and Halevy, I. (2021). Strong Local, Not Global, Controls on marine Pyrite Sulfur Isotopes. *Sci. Adv.* 7 (9), eabb7403. doi:10.1126/sciadv.abb7403

Paytan, A., and Griffith, E. M. (2007). Marine Barite: Recorder of Variations in Ocean export Productivity. *Deep Sea Res. Part Topical Stud. Oceanogr.* 54 (5-7), 687–705. doi:10.1016/j.dsr2.2007.01.007

Paytan, A., Mearon, S., Cobb, K., and Kastner, M. (2002). Origin of marine Barite Deposits: Sr and S Isotope Characterization. *Geol* 30(8), 747–750. doi:10.1130/0091-7613(2002)030<0747:oombds>2.0.co;2

Pellerin, A., Antler, G., Holm, S. A., Findlay, A. J., Crockford, P. W., Turchyn, A. V., et al. (2019). Large Sulfur Isotope Fractionation by Bacterial Sulfide Oxidation. *Sci. Adv.* 5 (7), eaaw1480. doi:10.1126/sciadv.aaw1480

Reeburgh, W. S. (1976). Methane Consumption in Cariaco Trench Waters and Sediments. *Earth Planet. Sci. Lett.* 28 (3), 337–344. doi:10.1016/0012-821x(76)90195-3

Reynolds, M. A., Gleeson, S. A., Creaser, R. A., Friedlander, B. A., Haywood, J. C., Hnatyshin, D., et al. (2021). Diagenetic Controls on the Formation of the Anarraaq Clastic-Dominated Zn-Pb-Ag Deposit, Red Dog District, Alaska. *Economic Geology* 116 (8), 1803–1824. doi:10.5382/econgeo.4849

Richardson, J. A., Keating, C., Lepland, A., Hints, O., Bradley, A. S., and Fike, D. A. (2019). Silurian Records of Carbon and Sulfur Cycling from Estonia: The Importance of Depositional Environment on Isotopic Trends. *Earth Planet. Sci. Lett.* 512, 71–82. doi:10.1016/j.epsl.2019.01.055

Rickard, D. (2012). "The Evolution of the Sedimentary Sulfur Cycle," in *Sulfidic Sediments and Sedimentary Rocks*, 685–766. doi:10.1016/b978-0-444-52989-3.00017-9

Ries, J. B., Fike, D. A., Pratt, L. M., Lyons, T. W., and Grotzinger, J. P. (2009). Superheavy Pyrite (34Spyr > 34SCAS) in the Terminal Proterozoic Nama Group, Southern Namibia: A Consequence of Low Seawater Sulfate at the Dawn of Animal Life. *Geology* 37 (8), 743–746. doi:10.1130/g25775a.1

Seal, R. R., Alpers, C. N., and Rye, R. O. (2000). Stable Isotope Systematics of Sulfate Minerals. *Rev. Mineral. Geochem.* 40(1), 541–602. doi:10.2138/rmg.2000.40.12

Sim, M. S., Ono, S., and Hurtgen, M. T. (2015). Sulfur Isotope Evidence for Low and Fluctuating Sulfate Levels in the Late Devonian Ocean and the Potential Link with the Mass Extinction Event. *Earth Planet. Sci. Lett.* 419, 52–62. doi:10.1016/j.epsl.2015.03.009

Smith, M. T., Dickinson, W. R., and Gehrels, G. E. (1993). Contractional Nature of Devonian-Mississippian Antler Tectonism along the North American continental Margin. *Geol* 21(1), 21–24. doi:10.1130/0091-7613(1993)021<0021:cnodma>2.3.co;2

Torres, M. E., Brumsack, H. J., Bohrmann, G., and Emeis, K. C. (1996). Barite Fronts in continental Margin Sediments: A New Look at Barium Remobilization in the Zone of Sulfate Reduction and Formation of Heavy Barites in Diagenetic Fronts. *Chem. Geol.* 127(1-3), 125–139. doi:10.1016/0009-2541(95)00090-9

Torres, M. E., Bohrmann, G., Dubé, T. E., and Poole, F. G. (2003). Formation of Modern and Paleozoic Stratiform Barite at Cold Methane Seeps on continental Margins. *Geol.* 31(10), 897–900. doi:10.1130/G19652.1

Turchyn, A. V., and Schrag, D. P. (2006). Cenozoic Evolution of the Sulfur Cycle: Insight from Oxygen Isotopes in marine Sulfate. *Earth Planet. Sci. Lett.* 241 (3-4), 763–779. doi:10.1016/j.epsl.2005.11.007

Wang, Z. C., and Li, G. Z. (1991). Barite and Witherite Deposits in Lower Cambrian Shales of South China; Stratigraphic Distribution and Geochemical Characterization. *Econ. Geol. Bull. Soc. Econ. Geol.* 86(2), 354–363. doi:10.2113/gsecongeo.86.2.354

Wood, R. S., Lepland, A., Ogliore, R. C., Houghton, J., and Fike, D. A. (2021). Microscale δ34S Heterogeneities in Cold Seep Barite Record Variable Methane Flux off the Lofoten-Vesterålen Continental Margin, Norway. *Earth Planet. Sci. Lett.* 574, 117164. doi:10.1016/j.epsl.2021.117164

Xu, L., Lehmann, B., Mao, J., Zheng, W., Ye, H., and Li, H. (2016). Strontium, Sulfur, Carbon, and Oxygen Isotope Geochemistry of the Early Cambrian Strata-Bound Barite and Witherite Deposits of the Qinling-Daba Region, Northern Margin of the Yangtze Craton, China. *Econ. Geol.* 111(3), 695–718. doi:10.2113/econgeo.111.3.695

Yan, H., Pi, D., Jiang, S.-Y., Hao, W., Cui, H., Robbins, L. J., et al. (2020). Hydrothermally Induced 34S Enrichment in Pyrite as an Alternative Explanation of the Late-Devonian Sulfur Isotope Excursion in South China. *Geochim. Cosmochim. Acta* 283, 1–21. doi:10.1016/j.gca.2020.05.017

Zan, B., Yan, J., Liu, S., Mou, C., and Ran, B. (2020). Llandovery (Lower Silurian) Nodular Barite from the Northern Margin of Yangtze Block, South China, and its Paleoceanographic Implications. *Palaeogeogr. Palaeoclimatol. Palaeoecol.* 537, 109415. doi:10.1016/j.palaeo.2019.109415

Zhang, F., Dahl, T. W., Lenton, T. M., Luo, G., Shen, S.-z., Algeo, T. J., et al. (2020). Extensive marine Anoxia Associated with the Late Devonian Hangenberg Crisis. *Earth Planet. Sci. Lett.* 533, 115976. doi:10.1016/j.epsl.2019.115976